CIRCULARITY OF THE *INTERSTELLAR BOUNDARY EXPLORER* RIBBON OF ENHANCED ENERGETIC NEUTRAL ATOM (ENA) FLUX

H. O. Funsten[1], R. DeMajistre[2], P. C. Frisch[3], J. Heerikhuisen[4], D. M. Higdon[1], P. Janzen[5], B. A. Larsen[1],
G. Livadiotis[6], D. J. McComas[6,7], E. Möbius[1,8], C. S. Reese[9], D. B. Reisenfeld[5], N. A. Schwadron[8], and E. J. Zirnstein[4]

[1] Los Alamos National Laboratory, Los Alamos, NM 87545, USA; hfunsten@lanl.gov, dhigdon@lanl.gov, balarsen@lanl.gov
[2] Applied Physics Laboratory, Johns Hopkins University, Laurel, MD 20723, USA; Bob.DeMajistre@jhuapl.edu
[3] Department of Astronomy and Astrophysics, University of Chicago, Chicago, IL 60637, USA; frisch@oddjob.uchicago.edu
[4] Department of Physics and Center for Space Physics and Aeronomic Research, University of Alabama,
Huntsville, AL 35899, USA; jacob.heerikhuisen@uah.edu, Eric.Zirnstein@uah.edu
[5] University of Montana, Missoula, MT 59812, USA; paul.janzen@umontana.edu, dan.reisenfeld@umontana.edu
[6] Southwest Research Institute, San Antonio, TX 78228, USA; george.livadiotis@swri.org, dmccomas@swri.edu
[7] Physics and Astronomy Department, University of Texas at San Antonio, San Antonio, TX 78249, USA
[8] University of New Hampshire, Durham, NH 03824, USA; eberhard.moebius@unh.edu, nschwadron@unh.edu
[9] Department of Statistics, Brigham Young University, Provo, UT 84602, USA; reese@stat.byu.edu

ABSTRACT

As a sharp feature in the sky, the ribbon of enhanced energetic neutral atom (ENA) flux observed by the *Interstellar Boundary Explorer* (*IBEX*) mission is a key signature for understanding the interaction of the heliosphere and the interstellar medium through which we are moving. Over five nominal *IBEX* energy passbands (0.7, 1.1, 1.7, 2.7, and 4.3 keV), the ribbon is extraordinarily circular, with a peak location centered at ecliptic $(\lambda_{\rm RC}, \beta_{\rm RC}) = (219°2 \pm 1°3, 39°9 \pm 2°3)$ and a half cone angle of $\phi_{\rm C} = 74°5 \pm 2°0$. A slight elongation of the ribbon, generally perpendicular to the ribbon center-heliospheric nose vector and with eccentricity ~ 0.3, is observed over all energies. At 4.3 keV, the ribbon is slightly larger and displaced relative to lower energies. For all ENA energies, a slice of the ribbon flux peak perpendicular to the circular arc is asymmetric and systematically skewed toward the ribbon center. We derive a spatial coherence parameter $\delta_{\rm C} \leqslant 0.014$ that characterizes the spatial uniformity of the ribbon over its extent in the sky and is a key constraint for understanding the underlying processes and structure governing the ribbon ENA emission.

Key words: ISM: atoms – ISM: kinematics and dynamics – ISM: magnetic fields – ISM: structure – Sun: heliosphere

Online-only material: color figures

1. INTRODUCTION

The first sky map of energetic neutral atoms (ENAs) from the outer heliosphere measured from the *Interstellar Boundary Explorer* (*IBEX*; McComas et al. 2009a) revealed the so-called ribbon, a circular arc of enhanced ENA emission that is superimposed on the globally distributed ENA flux (GDF) that varies slowly across the sky (McComas et al. 2009b). Fuselier et al. (2009) showed that the ribbon is narrow ($\sim 20°$) in width, and Funsten et al. (2009a) showed that it closely follows a circular arc spanning $\sim 143°$ in the sky and is centered at ecliptic coordinate $(\lambda, \beta) = (221°, 39°)$, the likely direction of the interstellar magnetic field (ISMF).

Because it is a sharp feature, the ribbon is a key signature for understanding the structure of the ENA emission region responsible for the ribbon as well as the interaction of the heliosphere and the interstellar medium (ISM) through which we are moving (McComas et al. 2009b; Schwadron et al. 2009). The center of the ribbon, which appears to be the fundamental direction that governs the overall structure responsible for the ribbon, lies in the vicinity of the average magnetic field direction between the Sun and nearby stars (Frisch et al. 2012). The first three years of *IBEX* observations have also shown a temporal decrease in the observed ribbon flux (McComas et al. 2012c) as well as a heliotail structure through which the ribbon might pass (McComas et al. 2013).

For detailed spectral analysis of the ribbon, Schwadron et al. (2011) separated the ribbon flux from the GDF by representing the ribbon flux as a Gaussian profile in radial angle from the center of the ribbon. The substantial difference in the spectral characteristics of the ribbon and GDF strongly suggested that they arise from fundamentally different source plasma populations. Additionally, this study estimated a strong ISMF magnitude of ~ 3.3 μG from pressure balance arguments, consistent with similar values inferred from models and simulations that do not rely on *IBEX* observations (Ratkiewicz & Grygorczuk 2008; Zank et al. 2013).

The location of the ribbon center as a critical ordering parameter of the ribbon structure, as well as the circularity retained over large length scales, serves as a critical test for more than a dozen hypotheses (e.g., McComas et al. 2011) about the location, structure, and dynamics of the source plasma as well as its transport processes that lead to the observation of the ribbon. Results of magnetohydrodynamic (MHD) simulations of the ISM-heliospheric interaction (e.g., Heerikhuisen & Pogorelov 2011; Pogorelov et al. 2011) are consistent with (1) the ribbon center as the likely direction of the ISMF and (2) the arc traced by the ribbon as the result of perturbation of the ISMF geometry by the heliosphere. The perturbed ISMF magnetic field direction $\boldsymbol{B}_P$ resulting in the ribbon is uniquely perpendicular to the radial line-of-sight vector $\hat{r}$ from the inner heliosphere, i.e., $\boldsymbol{B}_P \cdot \hat{r} \approx 0$ (e.g., Schwadron et al. 2009). Several hypotheses attribute the ribbon to a transport effect, such that the observed ribbon ENAs are the consequence of multiple charge exchange of source plasma ions and are generated at a different location than the source plasma population (McComas et al. 2009b,
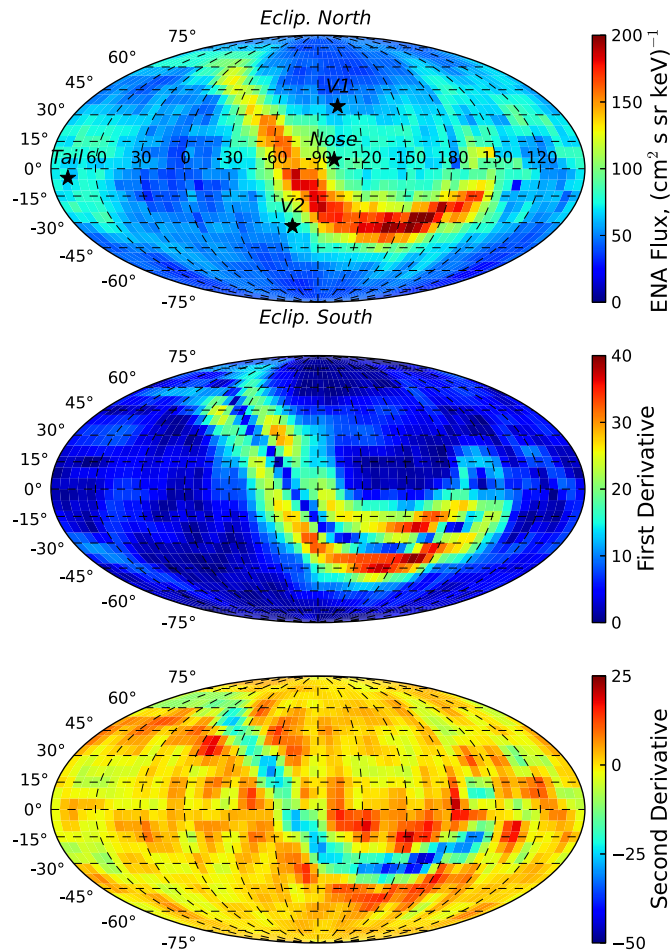
Figure 1. Ribbon is the most pronounced feature throughout the *IBEX* ENA flux maps. Top panel: the *IBEX* ENA flux map in ecliptic coordinates at nominal energy 1.1 keV acquired over *IBEX* orbits 11–150a, with the map centered on ecliptic $(-90°, 0°)$. For reference, *V1* and *V2* are the locations of the *Voyager 1* and *2* spacecraft in the sky. Middle panel: magnitude of the first derivative of the spatial flux distribution (top panel) using a Gaussian derivative filter, clearly showing the sides of the ribbon peak, which have the steepest slope within the flux map. Bottom panel: the map of the second derivative (using a Laplacian-of-Gaussian filter) of the flux map of the top panel reveals the spatial locations of flux peaks (negative values) and flux valleys (positive values); the ribbon is the dominant peak throughout the flux map.

(A color version of this figure is available in the online journal.)

Heerikhuisen et al. 2010; Chalov et al. 2010; Möbius et al. 2013; Schwadron and McComas 2013). Therefore, we define the ribbon formation region as the spatial volume in which the ribbon ENAs observed by *IBEX* are formed, which, because of potentially complex transport processes, may be different than the location of the source ion population that the ribbon ENAs represent; therefore, the properties of the observed ENA population (such as the spectral shape) may not represent the bulk plasma properties of the ribbon formation region.

With the completion of six sky maps over the first three years of the *IBEX* mission (McComas et al. 2012c), we have obtained much more statistically significant measurements of the ribbon fluxes observed within each of the five energy passbands spanning 0.71–4.3 keV of the *IBEX-Hi* ENA imager (Funsten et al. 2009b). The ribbon of enhanced flux is clearly observed as the dominant feature in Figure 1(a), which shows the full sky map of 1.1 keV ENA flux at $6° \times 6°$ resolution and centered on ecliptic $(-90°, 0°)$.

To understand the uniqueness of the ribbon as a sharp feature in the sky map, we apply two-dimensional (2D) Gaussian derivative filters that are routinely used for feature extraction in the analysis of noisy images (Canny 1986; Basu 2002). Figure 1(b) shows the gradient magnitude of the flux map derived using a Gaussian derivative for which the standard deviation of the 2D Gaussian filter was $6°$. The largest gradients are systematically observed on both sides of the ribbon, with maximum values on either side of the ribbon peak lying within a range of ~ 4 pixels ($24°$). This clearly illustrates the narrowness of the ribbon, consistent with the ribbon width initially measured by Fuselier et al. (2009).

Figure 1(c) shows the curvature coefficient of the flux map derived using a Laplacian-of-Gaussian (LoG) filter, again with a Gaussian standard deviation of $6°$. The LoG filter identifies peaks (negative values) and valleys (positive values), and the ribbon peak is clearly the dominant feature with maximum curvature throughout the image. We thus conclude that the location of the maximum flux along the ribbon curvature is a critical feature and an important metric associated with both the geometry and the uniformity of the underlying structure of the ribbon formation region.

In this study, we measure and analyze the ribbon location as a function of energy to understand the nature of this structure. As is apparent in both the middle and bottom panels of Figure 1, the largest gradients of ENA flux over the sky map lie in a direction perpendicular to the circular arc of the ribbon in the sky. Therefore, knowing that the ribbon is generally circular (Funsten et al. 2009a), this study utilizes a ribbon-centered reference frame from which analysis of the flux of the ribbon peak perpendicular to its arc is straightforward.

2. *IBEX* OBSERVATIONS IN THE RIBBON-CENTERED FRAME

We use ENA flux maps at $6° \times 6°$ resolution obtained from the *IBEX-Hi* neutral atom imager (Funsten et al. 2009b) for five energy passbands at nominal energies 0.7, 1.1, 1.7, 2.7, and 4.3 keV. The ENA flux maps, which are fully described in McComas et al. (2012c), span the first three years of the *IBEX* mission, include *IBEX* orbits 11 through 149, and are acquired from *IBEX* viewing in the ram direction only. The maps are corrected for both the Compton-Getting effect and for ENA extinction as calculated along their trajectories into the inner heliosphere.

For this analysis, we project the *IBEX* maps onto a ribbon-centered spherical coordinate system (azimuth, polar) = (θ, ϕ). In this system, the ribbon center lies nearly at $(0°, 0°)$ and ϕ corresponds to the angle between a point in the sky and $(0°, 0°)$. The azimuth angle θ ranges from $0°$ to $360°$ around the ribbon center, and the heliospheric nose direction at ecliptic $(\lambda, \beta) = (259°, 5°)$ (McComas et al. 2012a; Bzowski et al. 2012; Möbius et al. 2012) is located along the $\theta = 0°$ axis.

Based on the results of Funsten et al. (2009a), the maps shown in Figure 2 at nominal energies 0.7–2.7 keV are centered on ecliptic $(221°, 39°)$. In this study, we find that the ribbon at 4.3 keV appears at a different location from the lower energies, so we center the 4.3 keV map on ecliptic $(216°, 32°)$. These two map centers are separated by $8°.1$, slightly larger than the $6°.5$ FWHM intrinsic resolution of the *IBEX-Hi* ENA imager. In each of these rotated frames, the ribbon center derived at each energy passband lies at nearly $(0°, 0°)$, and the ribbon flux peak is generally found within the polar angle range $70° < \phi < 85°$.
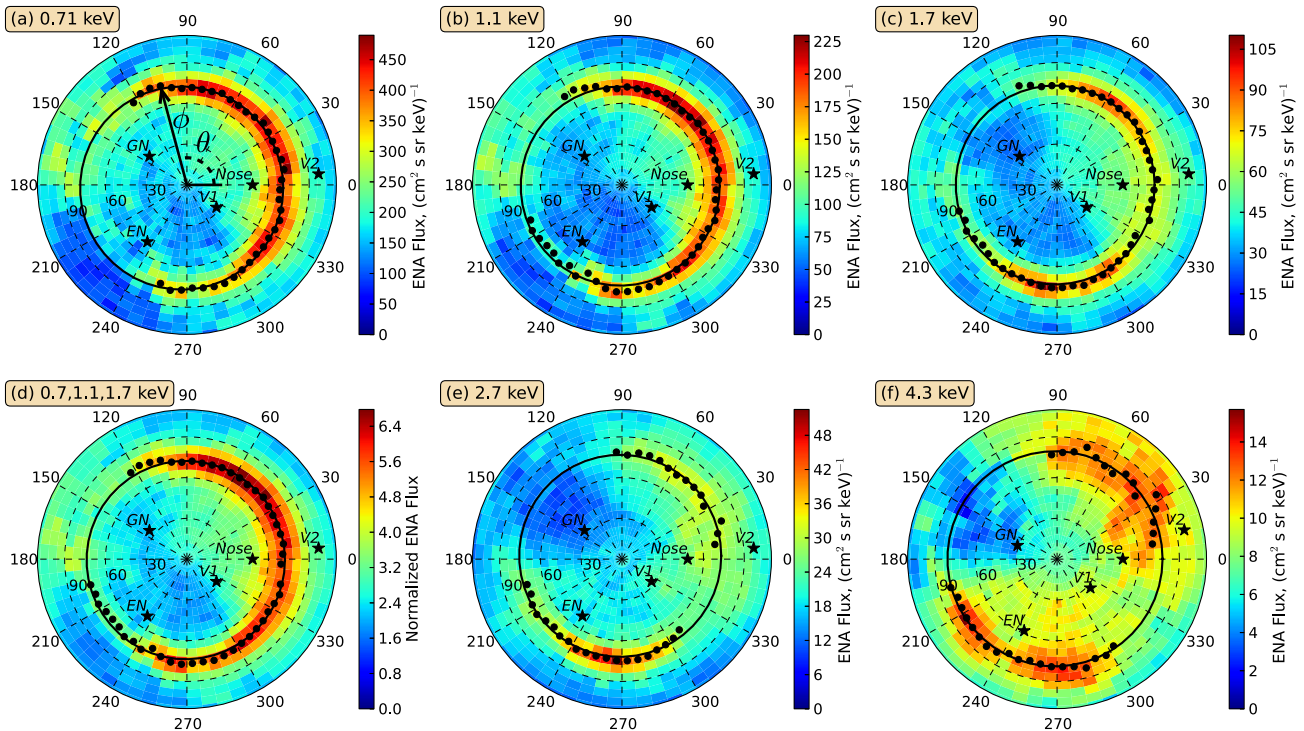
Figure 2. *IBEX* ENA flux maps are rotated into a common ribbon-centric reference frame with the heliospheric nose located along $\theta = 0°$ (θ and ϕ are defined in (a)). Panels (a)–(e) are centered on ecliptic (221°, 39°), whereas the highest energy (4.3 keV) flux map (f) is centered on ecliptic (216°, 32°). Panel (d) is a composite of three energy passbands linearly combined after normalizing each map to the 75th percentile flux value. Each black point is the location of the maximum ENA flux of the ribbon for an individual 6° azimuthal sector, derived using a Gaussian fit to the ribbon flux along polar angle ϕ. The black lines are circular fits to the black points based on the derived parameters of Table 1. The following directions are noted in each map for reference: *EN*, ecliptic north, *GN*, Galactic north, *V1*, *Voyager 1*, *V2*, *Voyager 2*, *Nose*, heliospheric nose.

(A color version of this figure is available in the online journal.)

For improved statistics, we linearly combine the maps at nominal energies 0.7, 1.1, and 1.7 keV by normalizing the fluxes of each individual map to its 75th percentile flux value and subsequently adding the fluxes of all three maps at each pixel. Normalizing to the 75th percentile flux value minimizes the influence of anomalously high flux pixels on the normalization. Figure 2(d) shows the composite 0.71–1.7 keV map.

In the rotated frames of Figure 2, the flux of the ribbon peak as a function of polar angle ϕ is reasonably represented by a Gaussian distribution (Schwadron et al. 2011). For each 6° azimuthal sector in this rotated frame, we first obtain from the flux map the 6° polar bin of maximum ribbon flux within a polar angle range of $60° \leqslant \phi \leqslant 90°$ for nominal energies 0.7–2.7 keV and within a range $60° \leqslant \phi \leqslant 102°$ for 4.3 keV, for which the ribbon peak is wider with possible excursions beyond 90°. Next, a Gaussian function $F = A + B\exp(-(\phi - \phi_{\mathrm{MAX}})^2/(2s^2))$ was fit to a total of seven contiguous polar pixels centered on the polar pixel of maximum flux. These seven polar pixels span 42° in polar angle, which is significantly broader than the FWHM of the peak. The fit parameters were ENA intensities A and B, the polar angle of maximum flux ϕ_{MAX}, and the standard deviation s of the Gaussian distribution. We thus obtain values $\phi_{\mathrm{MAX}}(\theta)$ and $s(\theta)$ as a function of the 6°-wide azimuthal sector θ.

A limited number of azimuthal sectors of the ribbon were excluded from this analysis using three criteria. First, *IBEX* persistently views one region of the sky through the terrestrial magnetosphere, whose ENA emission can be substantial (McComas et al. 2012b) and interferes with observation of the ENA flux from the outer heliosphere. In the rotated frames of Figure 2, the segment of the ribbon spanning azimuthal angles 126°–192° is obstructed by the magnetosphere and was

therefore excluded from the analysis. Second, 23 azimuthal sections over all energies (∼8% of the data) were excluded because the error of the derived polar angle ϕ_{MAX} of the location of maximum flux exceeded 2° for 0.7–2.7 keV and 3° for 4.3 keV. Third, a total of 13 azimuthal sections over all energies (∼4% of the data) were removed because of low ribbon flux, e.g., the Gaussian fit yielded $B/A < 0.05$. The black points in Figure 2 show the remaining polar angles of maximum ENA ribbon flux derived from the Gaussian fit.

2.1. Geometrical Model of the Ribbon Peak

At each energy, the polar angles ϕ_{MAX} of maximum ENA flux around the ribbon were fit to equations for a circle, with the circle center and angular radius ϕ_C as the free parameters, and an ellipse, with the ellipse center, semi-major axis, semi-minor axis, and rotation angle of the semi-major axis as the free parameters. The rotation angle θ_E is defined as the angle (in a counterclockwise direction) between the heliospheric nose axis in Figure 2 and the semi-major axis of the ellipse, such that $\theta_E = 90°$ corresponds to the elongation of the ribbon in a direction perpendicular to the heliospheric nose-ribbon center vector. The results of the fits are listed in Table 1 for the circular fit and Table 2 for the elliptical fit, in which the ribbon centers are listed in ecliptic coordinates.

For the circular fit, the derived polar angle ϕ_C of the ribbon peak from the ribbon center is extraordinarily consistent over the energy range 0.7–2.7 keV. Furthermore, the standard deviation σ_C of ϕ_C, which includes both the error associated with the derivation of ϕ_{MAX} from the Gaussian fit and the observed variability of ϕ_{MAX} in azimuth (and thus represents an upper limit on its variability), is consistently small. Over the energy

Table 1
Derived Fit Parameters of Maximum Ribbon Flux to a Circle

ENA Energy	Fit to Circle			
(keV)	Ribbon Center (Ecliptic)		Peak Polar Angle	
	λ_{RC}	β_{RC}	ϕ_C	σ_C
0.7–1.7	220°.6	40°.0	73°.0	2°.1
0.7	218°.5	43°.1	74°.8	1°.4
1.1	220°.3	40°.5	73°.3	2°.4
1.7	219°.6	39°.8	73°.2	1°.7
2.7	217°.9	37°.7	74°.4	2°.2
4.3	214°.2	32°.4	79°.2	3°.0

range 0.7–2.7 keV, ϕ_C ranges from 73°.1 to 74°.8 with a standard deviation $\sigma_C \leqslant 2°.4$. At 4.3 keV, ϕ_C is larger (~5° larger radial angle), suggesting a wider ribbon, and its location is more variable ($\sigma_C = 3°.0$), but still less than half the fundamental imaging resolution (6°.5) of the *IBEX-Hi* ENA imager.

The results of fitting an ellipse to the polar angles ϕ_{MAX} of maximum ribbon flux are shown in Figure 3 and summarized in Table 2, where the standard deviation σ_E of the elliptical fit was derived from the variance between the measured maximum flux values $\phi_{MAX}(\theta)$ and the fitted ellipse. At each energy, the difference between the circle and ellipse center locations lies within σ_C, showing consistency between the two methods. Because the ellipse has two extra free parameters (rotation angle and eccentricity), we fully expect the ellipse to provide a more statistically accurate fit to the data. As expected, for all energy passbands, σ_E is consistently smaller than the standard deviation σ_C derived for the circular fit.

From the elliptical fit, the eccentricity lies in the range $0.22 \leqslant e \leqslant 0.34$ with the semi-major axis <5° larger than the semi-minor axis. This indicates a small but systematic elongation of the ribbon. For all ENA energies, the rotation angle of the major axis falls within a range $65° \leqslant \theta_E \leqslant 111°$ in the rotated coordinate system of Figure 2. In this frame, the vector direction between the ribbon center and the heliospheric nose lies along $\theta = 0°$. The ribbon is therefore consistently elongated in a general direction perpendicular ($\theta_E = 90°$) to the ribbon center-heliospheric nose vector direction. Thus, we summarize that the ribbon is well characterized by a circle but is slightly elongated in a general direction perpendicular to the vector between the ribbon center and the heliospheric nose.

Table 3 shows the mean parameters (weighted according to inverse variance) over all five energy passbands for the circular fits (Table 1) and elliptical fits (Table 2). We additionally performed statistical significance testing of each of these parameters relative to energy independence. For a p value > 0.05,

energy independence is likely, and the parameter can be considered a constant value over all energies. We find that all parameters can be considered constants over all energies (i.e., p value ≫ 0.05) except for two cases. First, the rotation angle θ_E varies substantially over the energies, and, with p value ~0, energy independence is highly unlikely. Second, the latitude location β_{RC} of the ribbon is unlikely to be energy independent for both the circular and elliptical fits; thus, both the circular and elliptical fits suggest that the longitude direction of the ribbon center is more strongly and significantly coupled over all measured energies than the latitude direction. We define a standard ribbon center location in ecliptic coordinates using the calculated (weighted) mean of the circular and elliptical results, $(\lambda_{RC}, \beta_{RC}) = (219°.2 \pm 1°.3, 39°.9 \pm 2°.3)$ and a characteristic circularity defined by the half cone angle of $\phi_C = 74°.5 \pm 2°.0$ of the circular fit. This analysis is a refinement of the ribbon center value derived from the first *IBEX* sky map of $(221°, 39°)$ (Funsten et al. 2009a).

The derived centers of the circular and elliptical fits are shown in Figure 4 in ecliptic coordinates. The center locations for 0.7–2.7 keV are clustered around ecliptic (219°.2, 39°.9), but at 4.3 keV the derived centers are offset by ~10° lower in ecliptic latitude and by ~5° in ecliptic longitude. The ~8° angle between the ribbon center at 4.3 keV and the ribbon center (219°.2, 39°.9) derived over all energies is slightly larger than the 5°.6 difference in the semi-major axes for these two energy ranges. This suggests that the growth of the ribbon at 4.3 keV is skewed in the same direction as the offset of the centers. Furthermore, this offset direction, like the elliptical distortion of the ribbon at this energy, is generally perpendicular to the direction toward the heliospheric nose.

Also shown in Figure 4 are the vector direction of the magnetic field $\mathbf{B}_{V1, HDR}$ in the heliosheath depletion region (HDR) measured at *Voyager 1* (Burlaga et al. 2013) and its antipode. As *Voyager 1* continues along its trajectory toward the ISM, we expect that the magnetic field will rotate from its present direction to align with the unperturbed ISMF direction. Although the ISMF polarity is not currently known, its estimated vector direction in the vicinity of the ribbon center (Heerikhuisen & Pogorelov 2011) suggests rotation of $\mathbf{B}_{V1, HDR}$ (rather than its antipode) toward the ribbon center. The vector direction of the ideal Parker spiral magnetic field at the location of *V1* (Burlaga et al. 2013) is also shown for reference.

2.2. Statistical Model of the Ribbon Peak

The analysis so far is based solely on the circular and elliptical fits to the interpolated polar angle locations (derived using a Gaussian fit) of the maximum ENA flux of the ribbon at each

Table 2
Derived Fit Parameters of Maximum Ribbon Flux to an Ellipse

ENA Energy	Fit to Ellipse						
(keV)	Ribbon Center (Ecliptic)		Rotation Angle[a], θ_E	Semi-major Axis, a	Semi-minor Axis, b	e	σ_E
	λ_{RC}	β_{RC}					
0.7–1.7	220°.7	39°.9	110°.4	75°.0	71°.0	0.32	1°.5
0.7	219°.8	42°.2	97°.4	74°.9	73°.2	0.22	1°.4
1.1	220°.6	40°.2	111°.3	75°.4	71°.0	0.34	1°.8
1.7	219°.9	39°.7	100°.0	74°.4	71°.8	0.26	1°.5
2.7	218°.8	37°.6	76°.3	75°.7	70°.9	0.35	1°.8
4.3	215°.5	32°.5	65°.3	80°.3	75°.7	0.33	2°.9

Note. [a] Relative to the ribbon center-heliospheric nose vector.

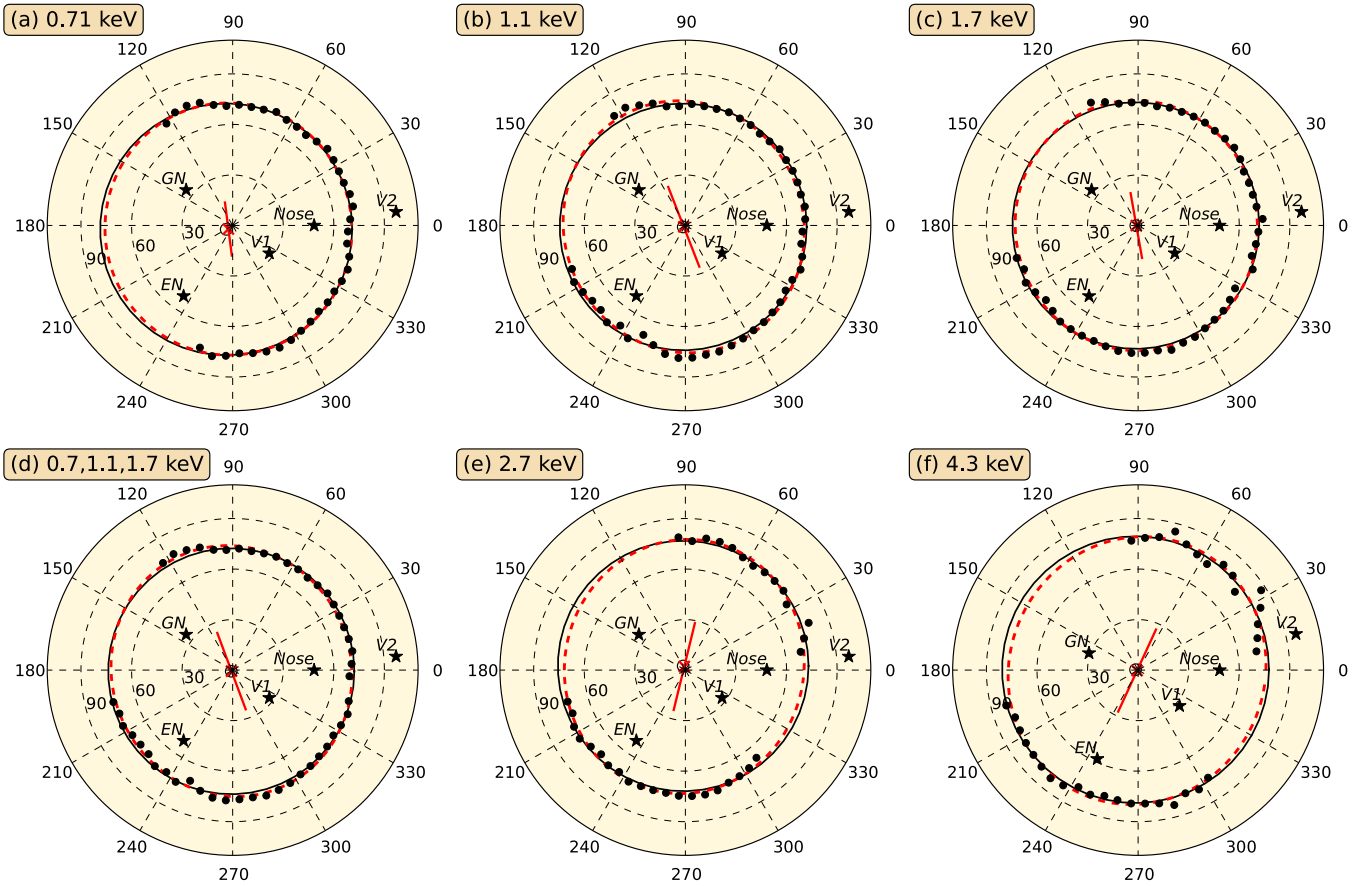**Figure 3.** Results of the circular fit (solid black lines) and the elliptical fit (red dashed lines) to the polar angle locations $\phi_{MAX}(\theta)$ of maximum ENA flux around the ribbon (black points). Panels (a)–(e) use flux maps centered on ecliptic (221°, 39°), whereas the results for 4.3 keV of panel (f) are centered on ecliptic (216°, 32°). The red line near the center of each panel spans the elliptical foci derived from the elliptical fit; therefore, the length of the red line is indicative of the elliptical eccentricity, and the angle of this red line relative to the axis along $\theta = 0°$ corresponds to the rotation angle θ_E of the derived ellipse, as shown in Figure 2. The derived circle centers (black points near (0°, 0°)) and elliptical centers (red circles near (0°, 0°)) lie close to the map centers in the respective rotated frames.
(A color version of this figure is available in the online journal.)

6° azimuthal sector. Here we construct an empirical flux model and develop a statistical framework using both the model and *IBEX* flux maps as input. This approach enables a more robust understanding of systematic variation of the entire ribbon peak as constrained by the observed variability of the ribbon intensity over nearby azimuthal and polar pixels, accounts for asymmetry of the ribbon peak in polar angle, and searches for higher modes of azimuthal variability of the ribbon peak location beyond the single stretching mode revealed by an elliptical fit. Assuming that the ribbon flux in the magnetospheric obstruction follows the magnitude and variability of the ribbon flux outside the obstruction, this analysis also enables interpolation of the ribbon flux through the magnetospheric obstruction.

This statistical model, which has substantial utility in image analysis (Winkler 2003), is described in detail in the Appendix. Briefly, the ribbon peak is modeled as a probability distribution function, the GDF is modeled as an ENA flux that varies slowly across the sky and underlies the ribbon flux, and the magnetospheric obstruction region is masked such that counts from this region do not influence the results of the statistical analysis. The statistical framework combines these three model components and an *IBEX* flux map within a Bayesian framework, such that individual parameters of the modeled ribbon flux and GDF flux are statistically constrained by their observed variability over the entire map (except for the magnetospheric obstruction). Statistical analysis was performed

for the composite 0.7–1.7 keV flux map as well as the 2.7 and 4.3 keV ENA flux maps in the ribbon-centric rotated frames of Figures 2(d)–(f).

Although the ribbon is the dominant ENA emission feature in the sky maps, other ENA emission features have been observed, such as the heliotail (McComas et al. 2013), which can overlap with the native ribbon emission. A non-ribbon feature can therefore introduce some uncertainty in the statistical analysis results if its ENA flux varies in polar angle ϕ in the vicinity of the ribbon. For our analysis, we assume negligible contribution from non-ribbon features to the measured ribbon flux. Furthermore, by assuming that the ribbon flux within the magnetospheric obstruction naturally follows the spatial variability of the ribbon flux outside of the obstruction, we use the statistical framework to interpolate the ribbon flux within the obstruction.

Figure 5 shows the resulting posterior estimates for 3000 realizations at each energy of the mean value $\bar{\phi}_{MAX}(\theta)$ (blue line) of the polar angle of maximum ribbon flux around the ribbon. The uncertainty (95% envelope) of $\bar{\phi}_{MAX}(\theta)$ is shown as the light turquoise band. Also shown for comparison are the results from Figure 3, in which the black points are the maximum ribbon peak locations $\phi_{MAX}(\theta)$ derived using a Gaussian fit, and the black and red lines are the fits of the black points to a circle and ellipse, respectively (Tables 2 and 3).

The ribbon peak locations estimated using the statistical analysis strongly indicate that the ribbon is not precisely

Table 3
Summary of Circular and Elliptical Fit Parameters and Statistical Test of Energy Independence

	Fit Parameter	Weighted Mean	Test of Energy Independence	
		(weight $= \sigma^{-2}$)	p-value	Test Rate
Circular fit	λ_{RC}	$218\overset{\circ}{.}6 \pm 2\overset{\circ}{.}0$	0.46	Highly likely ($\gg 0.05$)
	β_{RC}	$40\overset{\circ}{.}2 \pm 3\overset{\circ}{.}6$	0.015	Unlikely (< 0.05)
	ϕ_C	$74\overset{\circ}{.}5 \pm 2\overset{\circ}{.}0$	0.49	Highly likely ($\gg 0.05$)
Elliptical fit	λ_{RC}	$219\overset{\circ}{.}5 \pm 1\overset{\circ}{.}6$	0.36	Highly likely ($\gg 0.05$)
	β_{RC}	$39\overset{\circ}{.}7 \pm 3\overset{\circ}{.}0$	0.028	Unlikely (< 0.05)
	θ_E	95 ± 15	~ 0	Impossible ($\ll 0.05$)
	a	$75\overset{\circ}{.}4 \pm 1\overset{\circ}{.}8$	0.48	Highly likely ($\gg 0.05$)
	b	$72\overset{\circ}{.}2 \pm 1\overset{\circ}{.}7$	0.45	Highly likely ($\gg 0.05$)
	e[a]	0.31 ± 0.08	0.14	Likely (> 0.05)
Mean	λ_{RC}	$219\overset{\circ}{.}2 \pm 1\overset{\circ}{.}3$		
	β_{RC}	$39\overset{\circ}{.}9 \pm 2\overset{\circ}{.}3$		

Note. [a] Eccentricity errors are derived from propagation of the errors of a and b.
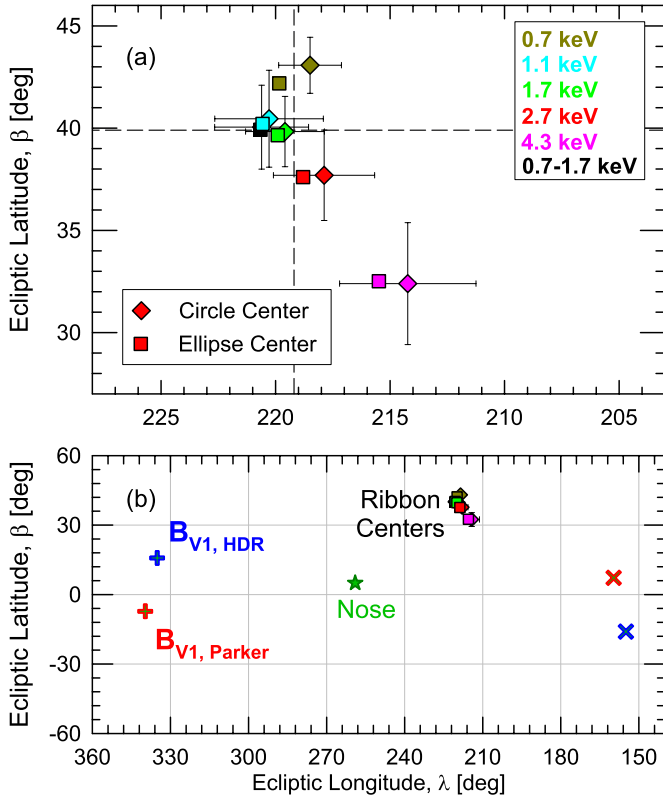

Figure 4. (a) Ribbon centers derived from the circular and elliptical fits to the ribbon flux maxima are shown in ecliptic coordinates for each energy passband and for the composite (0.7, 1.1, and 1.7 keV) passband. Longitude is shown in decreasing angle, similar to the flux map format of Figure 1, which reflects the viewing perspective from Earth. The ribbon center is therefore on the starboard side of outer heliosphere based on the upwind flow direction of the ISM through the heliosphere (McComas et al. 2013). The error bars shown for the center locations are equal to $\pm\sigma_C$ and $\pm\sigma_E$ from Tables 1 and 2, respectively. The dashed lines show the ribbon center ($219\overset{\circ}{.}2$, $39\overset{\circ}{.}9$) derived from the circular and elliptic fits over all energies (Table 3). (b) Circular and elliptical centers are shown in relation to the direction of the heliospheric nose at ecliptic (λ, β) = ($259\overset{\circ}{.}0$, $5\overset{\circ}{.}0$), which lies $50\overset{\circ}{.}0$ from the ribbon center defined at ecliptic ($219\overset{\circ}{.}2$, $39\overset{\circ}{.}9$). Also shown are the vector direction (+) of the magnetic field $\mathbf{B}_{V1, HDR}$ in the heliosheath depletion region (HDR) measured at *Voyager 1* (*V1*; Burlaga et al. 2013) and its antipode (×), and the vector direction (+) of the magnetic field $\mathbf{B}_{V1, Parker}$ of the Parker spiral at *V1* and its antipode (×), all of which have been translated into the ecliptic frame for comparison with the vector directions of the nose and ribbon centers from the Sun.

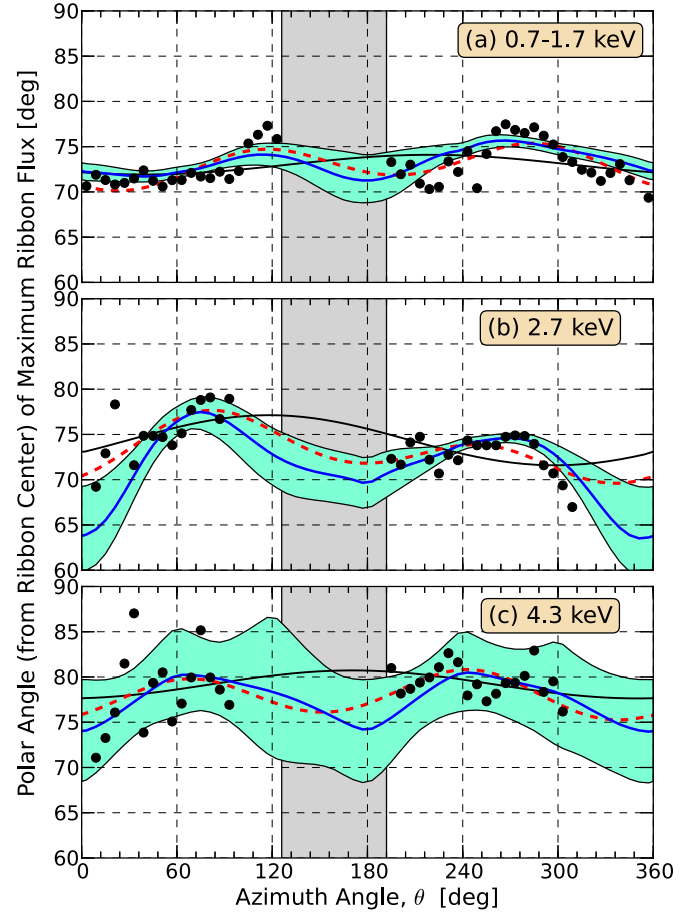(A color version of this figure is available in the online journal.)

Figure 5. Estimated locations of the maximum intensity of the ribbon flux as a function of azimuthal angle around the ribbon were derived using the statistical analysis of the flux map (see text and Appendix). The blue line shows the posterior mean location $\bar{\phi}_{MAX}(\theta)$ of the maximum ribbon flux, and the light turquoise band spans the 95% uncertainty interval of $\bar{\phi}_{MAX}(\theta)$. The results in panels (a)–(c) were derived from the maps of Figures 2(d)–(f), respectively, with (a) and (b) centered on ecliptic ($221°$, $39°$) and (c) 4.3 keV centered on ecliptic ($216°$, $32°$). The results of Figure 3 are also shown for comparison: the ribbon flux maxima $\phi_{MAX}(\theta)$ (black points), the circular fit to the black points (solid black line), and the elliptical fit to the black points (red dashed line). The gray vertical band represents the magnetospheric obstruction.

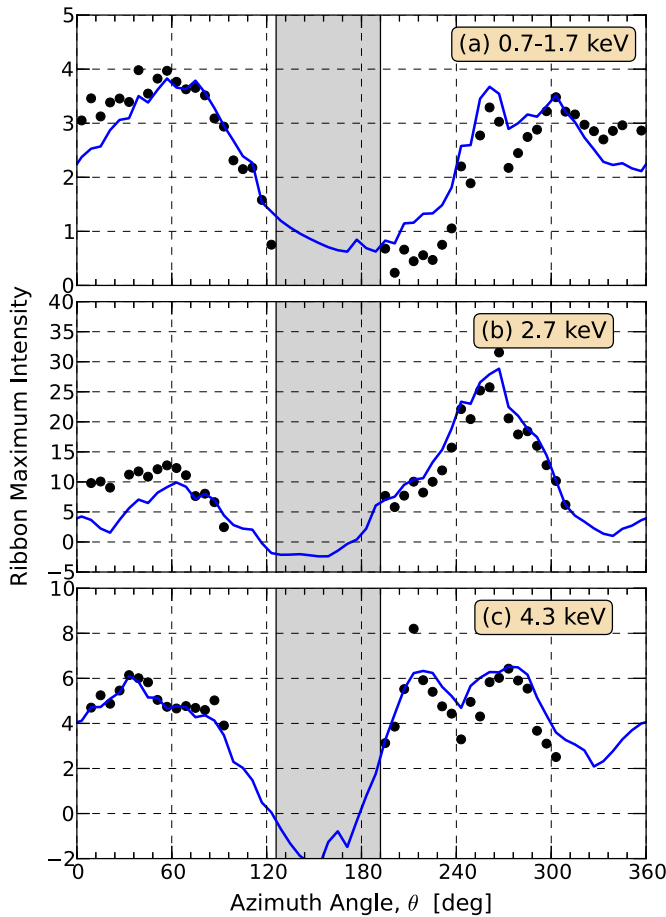(A color version of this figure is available in the online journal.)

Figure 6. Blue lines show the mean peak intensity of the plausible representations of the intensity function $I(\theta)$ obtained from the statistical analysis (as in Figure 5). For qualitative comparison, also shown are the maximum observed ribbon flux (black points), derived by subtracting constant GDF values of 2.8 normalized flux units (0.7–1.7 keV combined), 21 cm^{-2} s^{-1} sr^{-1} keV^{-1} (2.7 keV), and 7.5 cm^{-2} s^{-1} sr^{-1} keV^{-1} (4.3 keV) from the polar pixels of maximum flux at each azimuthal sector in Figure 2. As in Figure 5, the gray vertical band represents the magnetospheric obstruction. The statistical analysis predicts some ribbon ENA flux throughout the magnetospheric obstruction for 0.7–1.7 keV, but regions of no ribbon flux at 2.7 and 4.3 keV. The flux units for (b) and (c) are cm^{-2} s^{-1} sr^{-1} keV^{-1}; panel (a) has been normalized for the construction of a composite map from maps at the three different ENA energies. (A color version of this figure is available in the online journal.)

circular. However, for the composite 0.7–1.7 keV ENA map, the 95% confidence interval bands lie completely within the polar angle range 68°–77° over all azimuthal angles, consistent with the previous analysis that the ribbon in this energy range is nearly circular. However, $\bar{\phi}_{MAX}(\theta)$ closely follows (within ∼2°) the elliptical fit, illustrating that the statistical analysis of the 0.7–1.7 keV ENA flux map exhibits slight elongation of the ribbon in a similar direction as the elliptical fit.

At higher energies, the ribbon peak location deviates further from a circular representation and the 95% confidence interval band broadens, showing increased uncertainty of $\bar{\phi}_{MAX}(\theta)$. Nevertheless, for both 2.7 keV and 4.3 keV, $\bar{\phi}_{MAX}(\theta)$ generally follow the elliptical fit results, tracing a curve having two clear minima and two clear maxima, each approximately 180° from each other. Therefore, the statistical analysis clearly exhibits a mode characteristic of an elliptical-shaped ribbon, and no other higher order modes are apparent.

Figure 6 shows the results of the statistical analysis for the mean maximum ribbon flux intensity derived from the intensity

function $I(\theta)$ as a function of azimuthal angle θ. Also shown for qualitative comparison (black points) are the maximum measured ENA fluxes from Figure 2 at each azimuthal sector around the ribbon after subtraction of a constant value of the globally distributed flux at each energy. The variation of $I(\theta)$ with θ closely follows the envelope of maximum flux measured around the ribbon, showing agreement between the statistical results for the flux model and the observations.

Of particular interest is the interpolation by the statistical framework of the ENA ribbon flux within the magnetospheric obstruction, which, as previously mentioned, assumes that (1) non-ribbon features do not significantly contribute to the ribbon flux and (2) the ribbon flux inside the obstruction follows the observed spatial variability of the ribbon outside the obstruction. For the low-energy composite map (0.7–1.7 keV), the statistical analysis predicts ribbon ENA flux throughout the magnetospheric obstruction, reaching a minimum near ∼180°, near the magnetospheric obstruction boundary. However, at both 2.7 and 4.3 keV, the statistical analysis predicts negative values of ribbon flux within the magnetospheric obstruction, which we interpret as little or no ribbon flux, as well as the possible presence of other ENA emission features that may be superimposed on the ribbon such as the heliotail (McComas et al. 2013). Both the apparent completeness of the circular ribbon at low energies and the apparent depletion of ribbon ENA flux at higher energies within the magnetospheric obstruction are important constraints for correctly interpreting and understanding the ribbon and other features that are superimposed on the ribbon.

As described in the Appendix, the statistical framework derives a skewness parameter $\bar{\gamma}_1$ averaged over all azimuthal angles of the Gamma function kernel $k(\Delta\phi)$ representation of the ribbon peak for 3000 realizations at each energy range, where $\Delta\phi = \phi - \phi_{MAX}$ for each 6° azimuthal bin. The skewness parameter characterizes the systematic skewness over the entirety of the ribbon, where $\bar{\gamma}_1 < 0$ corresponds to a wider ribbon peak toward the ribbon's interior ($\phi < \bar{\phi}_{MAX}(\theta)$), $\bar{\gamma}_1 = 0$ corresponds to perfect symmetry, and $\bar{\gamma}_1 > 0$ corresponds to wider distribution outside of the ribbon ($\phi > \bar{\phi}_{MAX}(\theta)$). Figure 7(a) shows histograms of the resulting average posterior values of $\bar{\gamma}_1$ for the three energies. The range of $\bar{\gamma}_1$ spans −0.95 to −1.3, and the results for the 4.3 keV peak show a comparatively larger asymmetry and more variation in $\bar{\gamma}_1$. For reference, Figure 7(b) graphically shows the shape of the gamma function $k(\Delta\phi)$ for $\gamma_1 = -0.95$ and $\gamma_1 = -1.3$. Because the statistical analysis also derives an intensity and absolute peak width, the gamma distributions are shown as a function of relative polar angle centered on the ribbon maximum and on a relative flux scale. These results are strong evidence for a systematic skewness in $k(\Delta\phi)$ toward the ribbon center over all energies. We note that the characteristic asymmetric shape of the ribbon flux shown in Figure 7(b) is similar to the ribbon flux suggested by the non-heliospheric hypothesis of the origin of the ribbon posed by Grzedzielski et al. (2010).

This sharp cutoff for ENA emission of the ribbon exterior lies immediately inside of the great circle scribed by $\phi = 90°$ in Figure 2, suggesting a boundary or restriction of a physical process that underlies ENA emission from the ribbon formation region. Assuming that the ribbon center defines the true ISMF direction, then $\phi = 90°$ corresponds to the equator of the unperturbed ISMF geometry as well as the condition $\boldsymbol{B}_{ISM} \cdot \hat{r} = 0$. This suggests that a physical confinement process that results in a circular ring of ENA emission from a heliospheric-perturbed ISMF (along $\boldsymbol{B}_P \cdot \hat{r} = 0$, e.g., Schwadron et al.
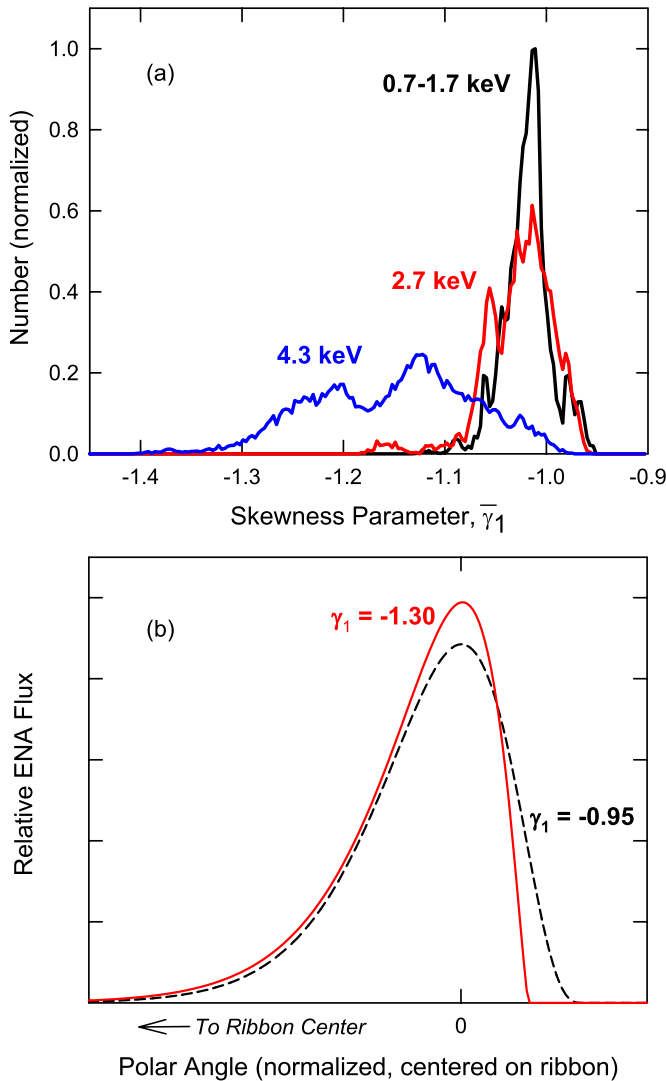
Figure 7. (a) Histograms of the average skewness parameter $\bar{\gamma}_1$ of the ribbon kernel function $k(\Delta\phi)$ over all azimuthal angles derived from 3000 realizations of the statistical analysis. (b) Shape of the gamma function representation of the ribbon peak corresponding to the range of skewness parameter values in panel (a). The ribbon peak is asymmetric and systematically skewed toward its interior (toward the ribbon center) for all three energy ranges.

(A color version of this figure is available in the online journal.)

2009) is not possible in the unperturbed ISM, perhaps due to the large distance from the Sun to locations of unperturbed ISM magnetic field or the absence of ISMF curvature which creates a directional preference for ENA emission toward the inner heliosphere.

3. DISCUSSION

3.1. Spatial Coherence of the Ribbon Emission Region

The ribbon ENA flux is a sharp feature, and the projection of the ribbon in the sky is extraordinarily circular. The key ordering parameter of the ribbon is its center at ecliptic (219°.2, 39°.9), which lies 50°.0 from the heliospheric nose defined at ecliptic (259°.0, 5°.0) (McComas et al. 2012a). This circular geometry, its subtle elongation, and its enlargement at 4.7 keV are important constraints for the multitude of hypotheses of the ribbon's origin (McComas et al. 2011, 2012c). Many of these models assume that the ordering parameter of the ribbon is the ISMF $\boldsymbol{B}_{\rm ISM}$ and that its direction is aligned with the center of the ribbon as

viewed from the inner heliosphere. If this is correct, then $\hat{\boldsymbol{B}}_{\rm ISM}$ lies at a substantial angle (50°.0) from the upwind flow direction of the ISM through the heliosphere.

The ribbon's sharpness, circularity, and size in the sky indicate that the physical processes that generate the ribbon are spatially uniform throughout the ribbon formation region, which may extend for hundreds of AU beyond the heliopause. The statistical variation $\sigma_{\rm C}$ listed in Table 1, which describes the uncertainty of the circular fit to the ribbon peak locations $\phi_{\rm C}(\theta)$, provides a quantitative constraint on the spatial and temporal variability of these underlying processes, which might arise from, for example, the draping geometry of the ISMF over the heliosphere (McComas et al. 2009a; Schwadron et al. 2009; Heerikhuisen et al. 2010; Chalov et al. 2010; Pogorelov et al. 2011), oscillation of the outer heliosheath configuration in response to solar cycle variations (Pogorelov et al. 2011), and turbulent magnetic field and plasma flow fluctuations in the ISM (Armstrong et al. 1995; Spangler et al. 2011).

To quantify the global spatial coherence of the ribbon, we introduce the coherence parameter $\delta_{\rm C}$, which is simply defined as the ratio of spatial variability (perpendicular to our line-of-sight viewing) to spatial size over the extent of the ribbon. Although $\delta_{\rm C}$ is a simplistic representation, its utility as a global observational constraint is powerful, providing upper limits on the spatial and temporal variability of the underlying physical processes that generate the ribbon, as well as stochastic processes such as turbulence and large-scale discontinuities or embedded structures in the ISM. Because we find that $\delta_{\rm C}$ is only moderately sensitive to the distance of the emission region from the Sun, it is likely to apply over spatial scales of hundreds of AU, as well as over timescales of decades based on traversal of these distances at an ISM Alfvén speed of $\sim$25 km s^{-1} ($\sim$5 AU yr^{-1}), derived using $B_{\rm ISM} = 3$ μG and a proton density of 0.07 cm^3 (Slavin & Frisch 2008).

The ribbon scribes an unexpectedly circular path over a large part of the sky. Thus, the spatial coherence parameter provides quantitative insight into the underlying spatial variability over the ribbon's vast spatial scale. Figure 8 schematically shows a slice through the ribbon formation region. We consider two lines of sight from the inner heliosphere to opposite sides of the ribbon that span $2\phi_{\rm C} \approx 149°$. The emission regions, which may have substantial radial thickness, lie at mean radial distances r_1 and r_2 from the Sun. The distance spanned by the chord that connects these points (blue line in Figure 8) is

$$d_{\rm C}(r_1, r_2, \phi_{\rm C}) = \left(r_1^2 + r_2^2 - 2r_1r_2\cos(2\phi_{\rm C})\right)^{0.5}. \quad (1)$$

We then estimate the variability of the chord length $d_{\rm C}$ based on the standard deviation $\sigma_{\rm C}$ of the polar angle of maximum ribbon flux from Tables 1 and 2. The derivative of $d_{\rm C}$ in Equation (1) with respect to $\phi_{\rm C}$ yields

$$\Delta d_{\rm C}(r_1, r_2, \phi_{\rm C}, \Delta\phi_{\rm C}) \approx \Delta\phi_{\rm C}\frac{2r_1r_2\sin(2\phi_{\rm C})}{d_{\rm C}(r_1, r_2, \phi_{\rm C})}. \quad (2)$$

We approximate $\Delta\phi_{\rm C}$ by adding the standard deviation $\sigma_{\rm C}$ in quadrature for each end of the chord, i.e., $\Delta\phi_{\rm C} \approx \sqrt{2}\,\sigma_{\rm C}$. The resulting ratio $\delta_{\rm C}$ of the characteristic spatial uncertainty $\Delta d_{\rm C}$ to the characteristic size scale $d_{\rm C}$ of the ribbon is

$$\delta_{\rm C}(r_1, r_2, \phi_{\rm C}, \sigma_{\rm C}) \approx \frac{\Delta d_{\rm C}}{d_{\rm C}} \approx \frac{2\sqrt{2}\sigma_{\rm C}r_1r_2\sin(2\phi_{\rm C})}{[d_{\rm C}(r_1, r_2, \phi_{\rm C})]^2}, \quad (3)$$

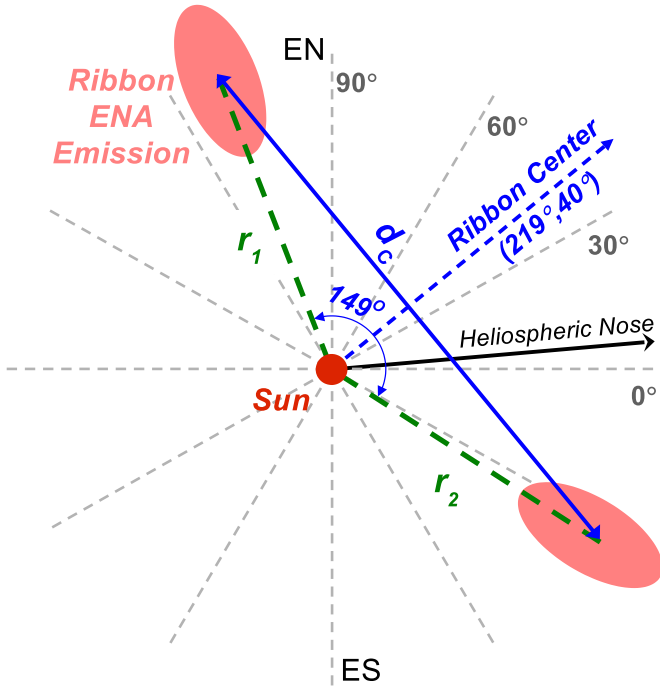which is a measure of the spatial coherence over the extent of the ribbon.

Figure 8. Schematic showing the chord (blue line) of distance d_C that spans opposite sides of the ribbon formation region (green blobs) and is the characteristic scale size of the ribbon system. The geometry uses an ecliptic reference frame (EN, ecliptic north, ES, ecliptic south, 0°, ecliptic plane) through ecliptic longitude ∼219°, for which opposite sides of the ribbon span a maximum 149° in ecliptic latitude. The heliospheric nose direction lies ∼39° out of this plane but is included for illustrative purposes.

(A color version of this figure is available in the online journal.)

The radial distance to and thickness of the ENA formation region are not known and may be different around the ribbon. Thus, we assess the sensitivity of the spatial coherence parameter δ_C on the radial distance to the ribbon formation region by assuming that at opposite sides of the ribbon, the ribbon emission regions are located at distances r_1 and r_2 from the inner heliosphere (as shown in Figure 8). Substituting $\beta = r_2/r_1$ yields

$$\delta_C(\beta, \phi_C, \sigma_C) \approx \frac{2\sqrt{2}\sigma_C\beta\sin(2\phi_C)}{1 + \beta^2 - 2\beta\cos(2\phi_C)}, \tag{4}$$

which shows that δ_C is independent of the absolute distance from the inner heliosphere to the ribbon formation region. Equation (4) can be written as

$$\delta_C(\beta, \phi_C, \sigma_C) \approx 2\sqrt{2}\sigma_C\sin(2\phi_C)\frac{\beta}{[\beta - \cos(2\phi_C)]^2 + \sin^2(2\phi_C)} \tag{5}$$

with derivative

$$\frac{\partial}{\partial\beta}\delta_C(\beta, \phi_C, \sigma_C) \approx 2\sqrt{2}\sigma_C\sin(2\phi_C)$$
$$\times \frac{1 - \beta^2}{\{[\beta - \cos(2\phi_C)]^2 + \sin^2(2\phi_C)\}^2}. \tag{6}$$

Therefore, δ_C reaches a maximum value δ_{Cmax} when $\beta = 1$, which corresponds to $r_2 = r_1$, resulting in

$$\delta_{Cmax}(\phi_C, \sigma_C) = \sqrt{2}\sigma_C\cot(\phi_C) \tag{7}$$
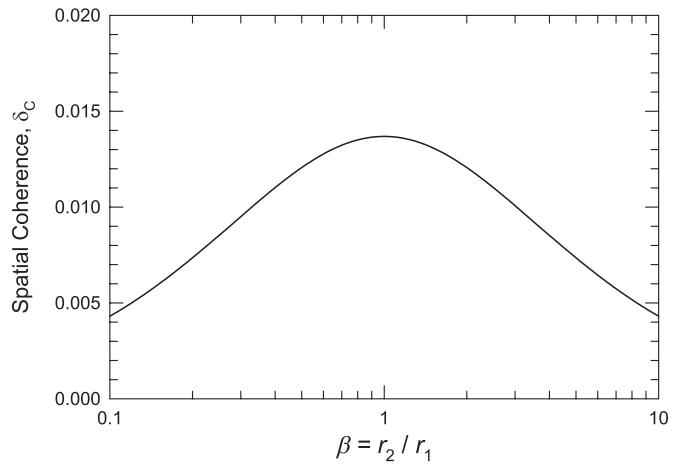
for σ_C in units of radians.

Figure 9. Unitless spatial coherence parameter δ_C of ENA flux from the ribbon is defined through Equations (3) and (4) as the systematic angular deviation of the ribbon from circularity relative to its angular extent in the sky. This figure shows that δ_C is not strongly sensitive to the radial distance from the ribbon emission region to the inner heliosphere, where r_1 and r_2 are the radial distances from the Sun to two discrete ENA emission points located at opposite sides of the ribbon (see Figure 8).

Figure 9 graphically shows δ_C as a function of β for $\phi_C = 74°.5$ and $\sigma_C = 2°$ from Table 3, for which $\delta_{Cmax} = 0.014$. δ_C retains expected symmetry, such that its value is the same at a fixed value of r_2/r_1 and its inverse r_1/r_2. Notably, δ_C is only moderately sensitive to r_2/r_1, for example, decreasing ∼65% (from ∼0.014 to 0.005) while r_2/r_1 spans a factor of 10 (from 1 to 10). Therefore, we conclude that δ_C is a key quantitative parameter that constrains the underlying physical properties responsible for ribbon uniformity and is minimally sensitive to the radial location of the emission region and its thickness. We note that δ_C represents an upper limit because σ_C includes uncertainty of the *IBEX* measurement of the ENA flux in addition to the ribbon's observed spatial variability.

The small value of the coherence parameter $\delta_C \leqslant 0.014$ illustrates that the structure underlying the ribbon formation region is extremely uniform over large distances. Using $\Delta d_C = \delta_C d_C$ and Equation (1) for d_C, we estimate the maximum spatial scales of variation in processes or structures responsible for observed variability in the ENA flux around the ribbon. With $\phi_C = 74°.5$ and $\delta_C \leqslant 0.014$, ENA emission in the vicinity of the heliopause at $r \sim 150$ AU results in a characteristic spatial variability $\Delta d_C \leqslant 4$ AU over a structure spanning $d_C \sim 290$ AU. Alternately, if the emission structure is located at a radial distance $r \sim 400$ AU from the Sun, then the characteristic spatial variability is only ∼11 AU over a structure spanning ∼770 AU.

3.2. Temporal Stability of the Ribbon Emission Region

As indicated by a small spatial coherence value $\delta_C \leqslant 0.014$, the properties of the structure that govern and generate the ribbon ENA emission are highly uniform over large spatial scales. However, the ENA sky maps are not snapshots in time because the ENA travel time from source to detection is energy dependent; from a common emission location, the travel time of an ENA at energy E_1 is a factor of $(E_2/E_1)^{1/2}$ slower than an ENA at higher energy E_2. Furthermore, this system is dynamic: the Sun moves through the ISM at 23 km s⁻¹ (McComas et al. 2012a), and bulk solar wind properties that may represent the origin of the observed ENAs change over latitude and solar cycle. Thus, we must also consider the implications of time,

in particular the stability of the ribbon's spatial coherence over time.

The ribbon flux spanning the nominal energy passbands 0.7, 1.1, and 1.7 keV spatially overlap (e.g., Table 1), thus exhibiting spatial stability over both the measurement time (three years) and the time differences of ENA transport over the energy passbands. For this composite energy range, we define a minimum ENA energy of 0.52 keV (which corresponds to the lower half-width at half-maximum (HWHM) of the nominal 0.7 keV passband) and a maximum ENA energy of 2.5 keV (which is the upper HWHM of the nominal 1.7 keV passband). The transit times of 0.52 and 2.5 keV ENAs are shown in Figure 10 (top panel) as a function of the radial distance of their origin from the Sun. For this analysis we assume that the radial extent of the ENA formation region is the same throughout this energy range. The travel time from a common, localized emission source is 2.2 times longer for a 0.52 keV ENA compared to a 2.5 keV ENA.

We define the minimum ribbon stability time $\tau_S = \tau_M + \Delta\tau_T$ as the sum of the measurement time interval $\tau_M = 3$ yr and the transport time difference $\Delta\tau_T$ between the fastest and slowest ENAs emitted at the same time from a common ENA source region and detected at *IBEX*. We estimate $\Delta\tau_T$ by first assuming that the ENA emission source associated with the ribbon flux spans a radial thickness Δr_{ENA} along any radial line of sight through the ribbon. We then approximate $\Delta\tau_T$ as the difference of the emission-to-detection transit times of the fastest ENA (2.5 keV) from the inner boundary of the emission region and the slowest ENA (0.52 keV) from its outer boundary.

The resulting transport time difference $\Delta\tau_T$ of these ENAs is shown in Figure 10 (middle panel) as a function of the radial distance from the emission region's inner boundary to the Sun for several emission region thicknesses Δr_{ENA}. Except for the thickest ENA emission region ($\Delta r_{ENA} = 500$ AU) at inner emission region boundaries >300 AU, $\Delta\tau_T$ is less than the 11 yr solar cycle. For these cases, we therefore expect that any solar cycle effects that alter the ribbon flux and/or ribbon location in the sky should be observable within these three energy passbands. Assuming a common ENA emission source region for all energies, a dynamic change in ENA emission associated with the ribbon would be observed first at the highest energy and observed later at lower energies. For example, the small but significant difference in the location and size of the ribbon flux at 4.3 keV may indicate dynamic change over time in the physical properties underlying the ribbon formation region rather than spectral variation of ENA emission within a globally static structure.

Temporal change in the ribbon formation region driven by spatial or temporal dynamics embedded within or propagating through the ISM may be substantially more difficult to observe because of the slow speed at which these dynamic domains traverse the ribbon formation region. The speed of turbulence in the ISM is small (0.5–3 km s^{-1}, Hebrard et al. 1999; Frisch et al. 2011), and thus unlikely to contribute to any observed dynamics. However, the speed of a disturbance embedded in the ISM moving relative to the Sun (23 km s^{-1}, McComas et al. 2012a) is comparable to the speed of a disturbance propagating through the ISM, with an Alfvén speed of ~25 km s^{-1} (based on $B_{ISM} = 3$ μG and a proton density of 0.07 cm^3; Slavin & Frisch 2008). Thus, the range of speeds of such a disturbance as viewed in the heliospheric reference frame is ~0 km s^{-1} for a disturbance propagating upstream in the ISM and ~50 km s^{-1} moving downstream in the ISM. The most rapid apparent motion
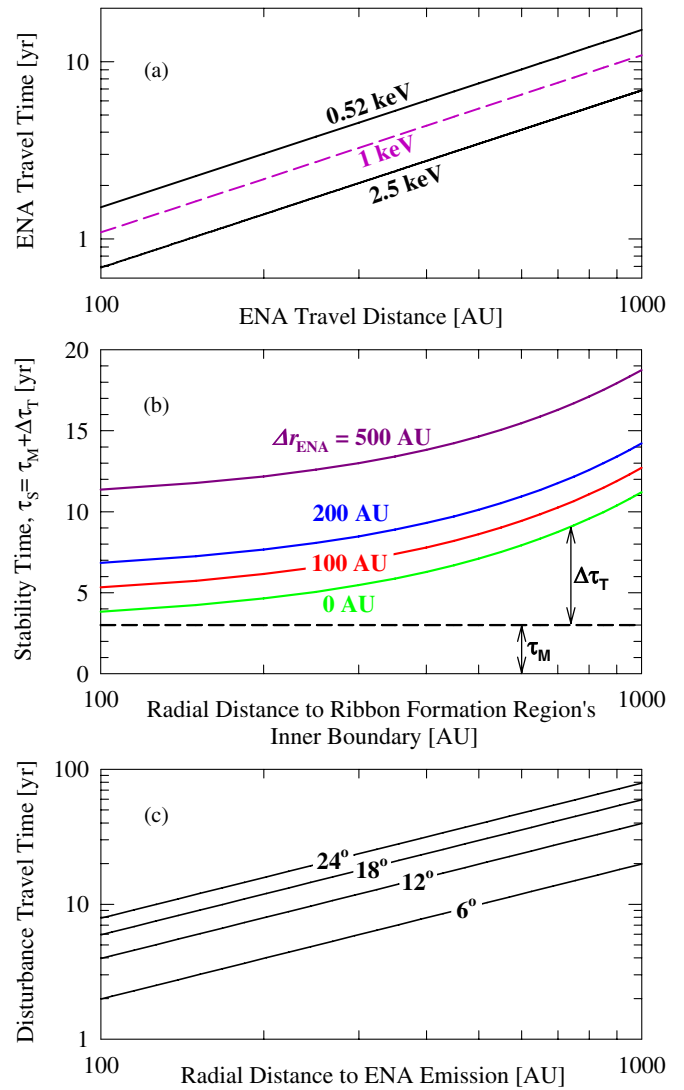

Figure 10. (a) ENA travel time as a function of radial distance at 0.52 and 2.5 keV, which correspond to the lower and upper energies spanned by the composite nominal energy passbands 0.7, 1.1, and 1.7 keV. For reference, the travel time for 1 keV hydrogen, which corresponds to the average bulk solar wind, is also shown (purple dashed line). (b) Time τ_S over which the spatial coherence $\delta_C < 0.014$ is observed is shown as a function of the inner boundary location of the ribbon formation region for several radial thicknesses Δr_{ENA} of this region. The stability time τ_S is the sum of the measurement interval $\tau_M = 3$ yr (light purple fill below black dashed line) and the difference in transport time $\Delta\tau_T$ of the slowest and fastest ENAs from a common ribbon formation region. (c) For a disturbance embedded in or propagating through the ISM moving 25 km s^{-1} perpendicular to an *IBEX* line of sight, the time to traverse 6° *IBEX* ENA flux map pixels is shown as a function of radial distance from the Sun. Such a disturbance might be embedded in the ISM, which moves ~23 km s^{-1} past the heliosphere, or propagating through the ISM, which has an Alfvén speed of ~25 km s^{-1}.

(A color version of this figure is available in the online journal.)

of dynamic change that modifies the ribbon shape or ENA flux should be observed (1) perpendicular to an *IBEX* line of sight and (2) perpendicular to the ribbon arc (i.e., along a single azimuthal sector in the ribbon-centric frame in Figure 2). Because the heliospheric nose lies in the interior of the ribbon, we reasonably expect a disturbance entrained in the ISM gas to follow the general flow of the ISM past the heliosphere, thus crossing the ribbon from its interior to its exterior.

Figure 10(c) shows the time for the leading edge of a disturbance at a specific radial distance from the Sun to

propagate angular distances from 6° to 24° in increments of 6°, which equals the resolution of the *IBEX* flux maps and is close to the 6°.5 intrinsic resolution of the *IBEX-Hi* ENA imager. We have assumed a propagation speed of 25 km s^{-1} perpendicular to the *IBEX* line of sight. The disturbance traversal across a single *IBEX* pixel occurs in less than three years if the disturbance lies at a radial distance ∼150 AU (the likely location of the heliopause) and within a decade if located ∼500 AU. Because the ENA signature of such a traversal should be spectrally broad and the disturbance spans a finite radial thickness Δr_{ENA} of ENA emission, the effects illustrated in Figure 10(b) result in a longer time evolution of the ENA signature than indicated in Figure 10(c).

The solar wind, which is a strong driver for mass and energy input into the heliosheath, is spatially variable in latitude (McComas et al. 2000), temporally variable over the ∼11 yr solar cycle, and impulsively dynamic with embedded transients such as coronal mass ejections at speeds much greater than 25 km s^{-1}. We expect solar wind transients and solar wind latitudinal variation to strongly influence the dynamics of plasma transport in the heliosheath, as well as the region of the nearby ISM perturbed by its interaction with the heliosphere. Therefore, temporal dynamics in the ribbon formation region are more likely to be observed if driven by the dynamics of the solar wind or solar cycle rather than by disturbances embedded in the ISM.

3.3. Testing of Models

The circular geometry of the ribbon is generally independent of the global geometry of other processes or structures that likely contribute to the ribbon ENA population, such as the hydrodynamic flow of the ISM plasma around the heliosphere (whose primary ordering parameter is the heliospheric nose direction) and the suprathermal solar wind (whose primary ordering is heliospheric latitude) that appears to be responsible for systematic spectral variation across the global ENA sky maps (Funsten et al. 2009b; Dayeh et al. 2011; Livadiotis et al. 2012). One of the leading hypotheses of the ribbon is the so-called "secondary" ENA emission source (McComas et al. 2009b) in which "primary" ENAs emitted from the supersonic and subsonic solar wind are ionized in the nearby ISM to form pick-up ions, which are subsequently re-emitted as "secondary" ENAs when these pick-up ions charge-exchange with a passing hydrogen atom. There are currently two models for the pick-up ion phase of the secondary ENA mechanism. The first (McComas et al. 2009b; Heerikhuisen et al. 2010; Chalov et al. 2010; Möbius et al. 2013) assumes that the pick-up ions with a pitch angle close to 90° do not scatter to an isotropic shell distribution as traditional theory predicts, but instead maintain a velocity distribution with pitch angles around 90°. Lines of sight that intersect this narrow velocity distribution (i.e., where the local perturbed magnetic field $\boldsymbol{B}_P$ is approximately perpendicular to the radial sight line from the sun $\hat{\boldsymbol{r}}$) then give rise to enhanced ENA flux. An alternative to the confinement of pick-up ions in velocity space is the spatial retention model developed by Schwadron and McComas (2013) that exploits the scattering of protons by Alfven waves for enhancement of ribbon ENA emission from regions where $\boldsymbol{B}_P \cdot \hat{\boldsymbol{r}} \approx 0$. Both of these models predict the same shape for the ribbon, with the only differences being in the magnitude of the flux and the radial thickness of the resulting ribbon.

Secondary source hypotheses, in which the ring of ENA emission observed by *IBEX* is governed by the condition
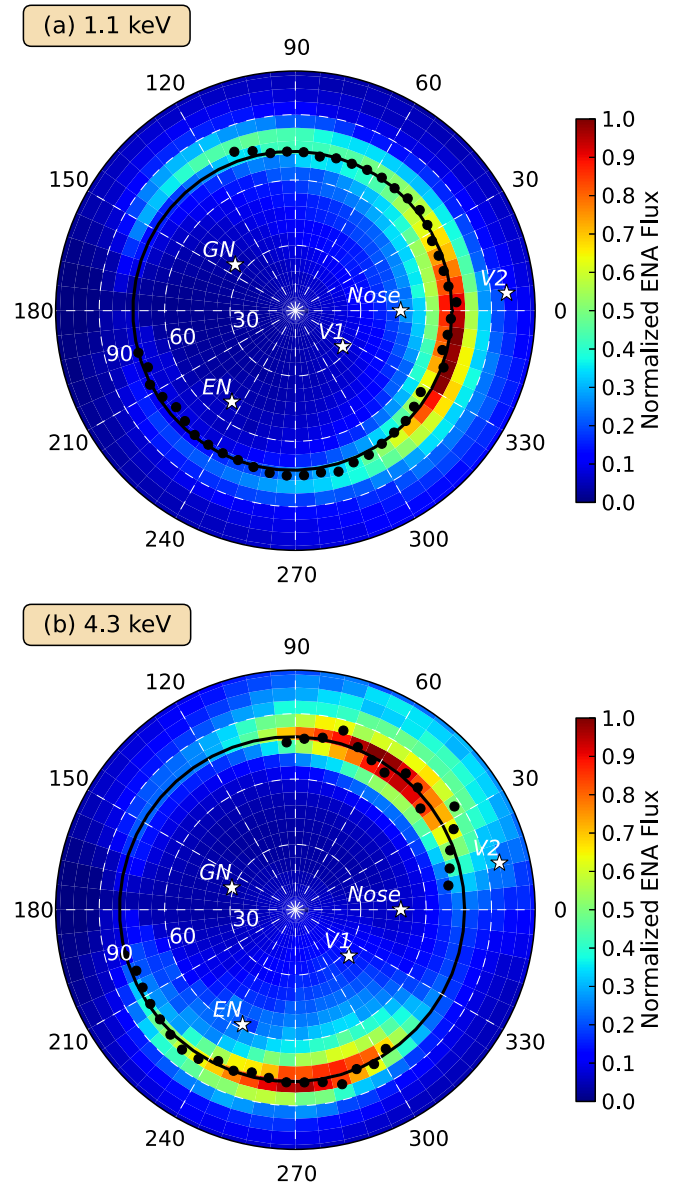

Figure 11. Simulations of the ENA flux from a "secondary" ENA source for 1.1 keV and 4.3 keV, both centered on ecliptic (220°.5, 40°). Also shown are the circular fits and polar angle locations of maximum ribbon flux for each energy. Although the simulations do not show an offset center at higher energy, they do exhibit a larger radius at higher energy, consistent with the observations.

(A color version of this figure is available in the online journal.)

$\boldsymbol{B}_P \cdot \hat{\boldsymbol{r}} = 0$, are well represented by MHD and kinetic simulations because $\boldsymbol{B}_{\mathrm{LISM}}$ is the global ordering parameter and the geometry of $\boldsymbol{B}_P$ is a straightforward simulation output. In Figure 11, we show simulated ENA flux from a secondary ENA emission source model with velocity space confinement for which $\boldsymbol{B}_{\mathrm{LISM}}$ far upstream (∼1000 AU) of the heliopause is 3 μG with an ecliptic vector direction (40°.5, −40°) whose antipode at (220°.5, 40°) is in close proximity to the ribbon center derived in this study. The simulations solve the coupled MHD and neutral, atomic hydrogen system of equations, so that the magnetic fields in the region where secondary ENAs are created have been correctly perturbed by their draping over, and advection around, the heliopause (Heerikhuisen et al. 2013).

The coherence parameter derived from the model results shown in Figure 11 uses the same calculation method as for the *IBEX* data, specifically, for each azimuthal sector a Gaussian

fit to the ENA flux using seven polar pixels centered on the polar pixel with maximum ribbon flux. Using only the azimuthal sectors in which the maximum ENA flux is at least 10% of the maximum flux in the map, the ribbon flux of Figure 11 yields $\delta_C = 0.053$ for 1.1 keV and $\delta_C = 0.044$ for 4.3 keV, both of which are ~ 3 times larger than that derived for the *IBEX* data ($\delta_C \leqslant 0.014$). Closer inspection of the model results shows a small but significant non-circularity to the ribbon that is the primary cause for the larger value of δ_C. This demonstrates the utility of δ_C for quantitatively comparing simulations with the flux maps.

Overlaid on the simulation results are the derived circular fit and polar locations of maximum ribbon flux ϕ_{MAX} at each energy (Figures 2(c) and (f)). The simulation shows the remarkable strength of the secondary ENA mechanism in reproducing not only the circularity of the ribbon but also its radius, the increase of radius at high energy, and the approximate locations of the bright and dim sections. In agreement with the analysis of the *IBEX* data shown in Figure 6, the simulations predict that the ribbon should extend into the magnetospheric obstruction and be dimmest in the anti-nose direction. While the circularity and radius of the simulated ribbon agree with the data at 4.3 keV, the steady-state simulation does not predict the offset center seen in the data. This suggests, as discussed in Section 3.2, that temporal effects may be responsible for the offset of the ribbon at the highest energies.

The circularity reflects the global uniformity of the perturbed ISMF $\boldsymbol{B}_P$ throughout the emission region of secondary ENAs. Its departure from circularity in the azimuthal range 210°–330° is due to the draping of the ISMF around the heliopause in the ENA source region beyond the heliopause (Schwadron et al. 2009; Pogorelov et al. 2011). We note that this elongation is perpendicular to the nose direction at 0° azimuth in the rotated frame of Figure 11 and in the same direction as the elongation of the ribbon observed in both the elliptical fit (Figure 3) and the results of the statistical analysis (Figure 5).

We expect that the large-scale uniformity of the ribbon is more representative of the ISM beyond the heliopause. If the ordering of the ribbon reflects the intrinsic structure of the ISM, then the spatial coherence δ_C represents an important constraint on the structure governing the intensity of ENA emission from the ribbon formation region. We conclude that the underlying uniform geometry of the source region of the observed ribbon ENA flux is (1) sufficiently far from the heliosheath that it is not strongly influenced by the hydrodynamic flow of the ISM around the heliosphere and (2) globally symmetric, and thus generally static in time, possibly reacting only to large-scale, long-term solar wind variations like those expected over the solar cycle.

For the secondary ENA emission source model of Figure 11 in which the ENA flux is partially due to our viewing geometry (i.e., of $\hat{\boldsymbol{r}}$ relative to $\hat{\boldsymbol{B}}_R$), δ_C thus indirectly constrains variation in the orientation of $\hat{\boldsymbol{B}}_R$ and, more globally, the symmetry and variability of the deflected ISMF around the heliosphere. Furthermore, because $\hat{\boldsymbol{B}}_R$ was the previously undisturbed $\boldsymbol{B}_{ISM}$ before its interaction with the heliosphere, variability in $\hat{\boldsymbol{B}}_R$ should likewise constrain the intrinsic fluctuations of $\boldsymbol{B}_{ISM}$.

4. SUMMARY

We summarize the main conclusions of this study.

1. Based on analysis of the maximum flux around the ribbon of enhanced ENA emission observed by *IBEX*, the ribbon is extraordinarily circular. We derive a standard ribbon center location at ecliptic $(\lambda_{RC}, \beta_{RC}) = (219°.2 \pm 1°.3, 39°.9 \pm 2°.3)$ with a half cone angle of $\phi_C = 74°.5 \pm 2°.0$. The direction from the inner heliosphere to the ribbon center is 50°.0 relative to the direction to the heliospheric nose.

2. A fit of the ribbon peak to an ellipse indicates a slight, systematic deviation from circularity across all ENA passbands (0.7–4.3 keV). This elongation has an eccentricity 0.31 ± 0.08 and in a direction that is generally perpendicular to the vector between the ribbon center and the heliospheric nose.

3. The ribbon at 4.7 keV is slightly displaced (by $\sim 8°$), larger (by $\sim 7°$ half cone angle), and more variable in location of peak emission (by a factor of ~ 2) relative to the ribbon at 0.7–1.7 keV.

4. A statistical analysis of the ribbon confirms the ribbon circularity with slight elongation characteristic of an ellipse and finds no other higher-order modes beyond elongation in one direction. The statistical analysis predicts ribbon flux in the magnetospheric obstruction for 0.7–1.7 keV and thus a complete ribbon. For 4.7 keV, the statistical analysis predicts an incomplete ribbon (no ribbon flux in one area of the magnetospheric obstruction).

5. The statistical analysis results indicate that the mean skewness parameter around the ribbon lies in the range -0.95 to -1.3. This corresponds to systematic skewing toward the ribbon center, such that the outer boundary of the ribbon peak is sharper than the interior boundary.

6. The ribbon formation region is coherent over a large spatial scale. We derive a unitless spatial coherence parameter $\delta_C = \Delta d_C/d_C$, where d_C is the distance between opposite sides of the circular ribbon and Δd_C is the mean spatial variability around the ribbon. We obtain $\delta_C \leqslant 0.014$ and find that δ_C is generally insensitive to both the radial distance to and radial thickness of the ribbon formation region. δ_C indirectly constrains variation in the orientation and global variability of the perturbed ISMF $\hat{\boldsymbol{B}}_R$ around the heliosphere, and because $\hat{\boldsymbol{B}}_R$ was the previously undisturbed $\boldsymbol{B}_{ISM}$ before its interaction with the heliosphere, variability in $\hat{\boldsymbol{B}}_R$ should likewise constrain the intrinsic fluctuations of $\boldsymbol{B}_{ISM}$.

7. Temporal changes in ENA emission resulting from variability of the solar wind over the solar cycle and large-scale transients in the solar wind should be observable in the *IBEX* all-sky maps.

8. The size and shape of the ribbon are quite similar over the energy range 0.7–1.7 keV, indicating a common emission source and stability over time.

APPENDIX

STATISTICAL FRAMEWORK AND ANALYSIS OF THE *IBEX* RIBBON FLUX

The ENA fluxes measured by the *IBEX-Hi* ENA imager are tenuous, thus yielding ENA flux maps with moderate signal-to-noise ratios (S/N). Figure 12 shows a sky map of calculated S/N values for the 1.7 keV ENA flux map of Figure 2(c) in the
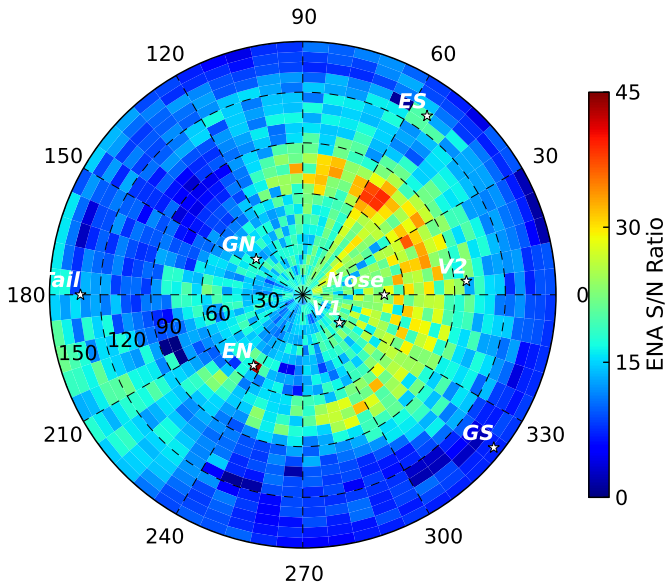
Figure 12. Sky map of the S/N calculated for the 1.7 keV ENA flux map, centered at (221°, 39°) as in Figure 2(c). The north and south ecliptic poles (labeled EN and ES, respectively) are viewed each spacecraft spin, resulting in the two localized regions of high S/N in these directions. Compared to Figure 2(c), the plotted polar angle range extends to 150° to show the ecliptic south pole.

(A color version of this figure is available in the online journal.)

same rotated reference frame that is centered on ecliptic (221°, 39°). The S/N in the region outside of the ribbon is ∼5–10. For the region in which ribbon flux is observed, which includes both the ribbon ENA flux and the globally distributed ENA flux, the S/N is in the range ∼10–40.

Our statistical approach is adapted from Bayesian image analysis (Besag et al. 1995; Winkler 2003). Such an approach can account for the moderate S/N range of the ribbon, the apparent structured and coherent ribbon ENA flux, and the substantial globally distributed flux that varies slowly over the sky maps, while providing a straightforward method to quantify uncertainties, particularly in the ribbon structure. In the projection of Figure 13, a circular ribbon corresponds to a horizontal line. Our objective is to understand how the flux measurements inform about the asymmetry of the ribbon peak and the polar location and magnitude of the ribbon flux maximum as a function of azimuth angle θ in the ribbon-centered frame, and in particular to search for higher modes of azimuthal variability beyond the single stretching mode revealed by an elliptical fit. We note that this analysis also enables interpolation of the ribbon flux through the magnetospheric obstruction. This statistical analysis was performed for the 2.7 and 4.3 keV ENA flux maps, as well as a composite (normalized) flux map consisting of the 0.7, 1.1, and 1.7 keV flux maps linearly combined after normalizing each individual map to its 75th percentile flux.

The statistical framework couples an ENA flux map $F_{IBEX}(\theta, \phi)$ as measured by *IBEX* (Figure 2) with a flux model. The flux model decomposes $F_{IBEX}(\theta, \phi)$ into three flux components using the same ribbon-centered frame as in Figure 2: the ENA flux $F_R(\theta, \phi)$ associated with the ribbon peak, a mask $F_M(\theta, \phi)$ of the magnetospheric obstruction, and the "residual" ENA flux $F_{RES}(\theta, \phi)$, which is primarily the slowly varying globally distributed flux (GDF) but may also contain some ribbon flux that is not well represented by $F_R(\theta, \phi)$, as well as other features in the sky maps that are neither ribbon nor GDF.

These components are linearly combined at each $6° \times 6°$ pixel, yielding

$$F_{IBEX}(\theta, \phi) = F_R(\theta, \phi) + F_M(\theta, \phi) + F_{RES}(\theta, \phi).$$

When combined with the *IBEX* flux map F_{IBEX} through the statistical framework, the prior models for the different components of the model flux, described next, determine the resulting decomposition, along with its uncertainty through the posterior distribution.

The first model component, the ribbon flux $F_R(\theta, \phi)$, is constructed using three functions that represent key features of the ribbon shape:

1. a kernel function $k(\phi - \phi_{MAX}(\theta))$ that represents the relative ribbon ENA flux as a function of polar angle ϕ for each $6°$ azimuthal sector,
2. a flux intensity function $I(\theta)$ that represents the total ENA flux (integrated over all polar angles) within each $6°$ azimuthal sector, and
3. a b-spline representation of $\phi_{MAX}(\theta)$ that represents the systematic variation of the polar angle of maximum ribbon flux over all azimuthal sectors (i.e., around the entirety of the ribbon).

Thus, the ribbon flux at any pixel (θ, ϕ) is a convolution of $I(\theta)$ and $k(\phi - \phi_{MAX})$,

$$F_R(\theta, \phi) = I(\theta)k(\phi - \phi_{MAX}(\theta)).$$

The intensity function is assigned a periodic random walk prior (Besag et al. 1995) over the 60 $6°$ azimuthal sectors, establishing continuity across azimuthal pixels, and limiting the intensity function variation between adjacent azimuthal pixels. The prior for $I(\theta)$ is controlled by a single precision parameter λ_I:

$$p(I|\lambda_I) \propto \lambda_I^{30} \exp\left\{-\frac{\lambda_I}{2}\sum_{i=1}^{60}(I_i - I_{i+1})^2\right\},$$

where the summation is periodic and therefore includes the term $I_{60} - I_1$. The precision parameter is given a rather uninformative Gamma prior

$$p(\lambda_I) \propto \exp\{-0.001\lambda_I\}, \quad \lambda_I > 0.$$

The kernel function $k(\Delta\phi)$, for which $\Delta\phi = \phi - \phi_{MAX}$, is a centered (i.e., zero-mean) gamma density function (Casella & Berger 2002)

$$k(\Delta\phi) = \frac{1}{\Gamma(\alpha)\omega}\left(\frac{\Delta\phi + \alpha\omega}{\omega}\right)^{\alpha-1}$$
$$\times \exp\left\{-\left(\frac{\Delta\phi + \alpha\omega}{\omega}\right)\right\}, \quad \Delta\phi > -\alpha\omega,$$

governed by two parameters: α controlling the shape and ω controlling the width. Wide uniform priors are specified for these two parameters

$$p(\alpha, \omega) \propto I[\alpha \in (0, 30); \omega \in (1, 30)].$$

From these two parameters, the skewness of $k(\phi - \phi_{MAX})$ can be computed directly as $\gamma_1 = 2\alpha^{-1/2}$. A skewness value $\gamma_1 = 0$ corresponds to a symmetric distribution, for which the gamma density function approaches the Gaussian approximation of
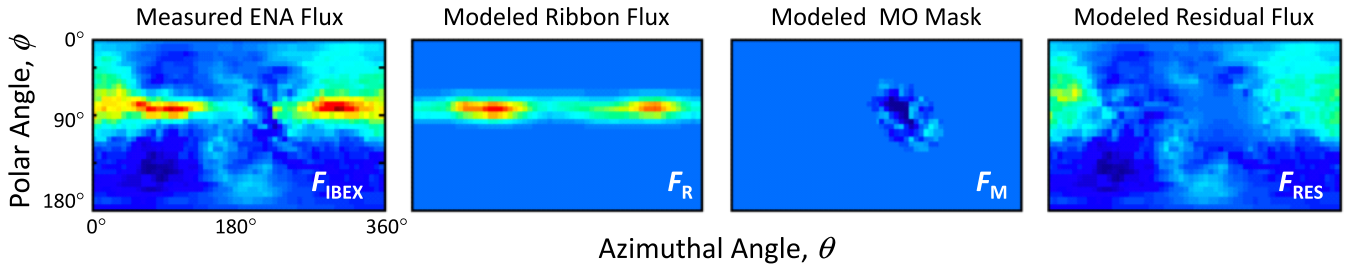
Figure 13. Posterior mean decomposition of measured fluxes F_{IBEX} into a model with three distinct flux components—ribbon (F_R), mask of magnetospheric obstruction (F_M), and residual flux (F_{RES}) that is predominantly the globally distributed flux. The framework described here statistically couples the measured and modeled flux maps; these panels show the decomposition of the *IBEX* 1.7 keV flux map into these three model components that results from the statistical analysis, using a ribbon-centered frame, with center $(221°, 39°)$. The center of the ribbon corresponds to $\phi = 0°$, i.e., the top of these rectangular images. Each image is an array of 60×30 pixels identical to those of Figure 2, with each pixel corresponding to $6° \times 6°$.

(A color version of this figure is available in the online journal.)

the ribbon flux peak used by Schwadron et al. (2011) and in Section 2.1 of this paper. Additionally, the sign of γ_1 indicates the direction of the skewness, and the flux model results overwhelmingly favor a negative skewness, i.e., a wider distribution on the interior of the ribbon peak, toward the ribbon center. For each $6°$ azimuthal sector, the kernel $k(\phi - \phi_{MAX})$ integrates to unity over the polar angle range $0°$–$180°$, so the value of $I(\theta)$ represents the total flux of the ribbon within a sector.

The collection of polar angles $\phi_{MAX}(\theta)$ of maximum ribbon flux are assumed to map out a closed line around the ribbon; this line of ribbon flux maxima $\phi_{MAX}(\theta)$ is modeled with periodic b-splines (Hastie et al. 2009, pp.139–189), allowing substantial deviations from a circular or elliptical shape. Here the b-spline basis elements, $b_k(\theta)$, are fixed, and $\phi_{MAX}(\theta)$ is determined by the coefficients u_k multiplying each basis element:

$$\phi_{MAX}(\theta) = \sum_{k=1}^{B} u_k b_k(\theta).$$

The $B = 10$ coefficients are given independent normal priors, with common variance $1/\lambda_u$

$$p(u|\lambda_u) \propto \lambda_u^{\frac{B}{2}} \exp\left\{-\frac{\lambda_u}{2} \sum_{k=1}^{B} u_k^2\right\},$$

with a diffuse gamma prior for the precision λ_u

$$p(\lambda_u) \propto \exp\{-0.001\lambda_u\}, \quad \lambda_u > 0.$$

This prior specification retains sufficient flexibility to identify periodic modes with a characteristic scale size less than $60°$, such that periodic modes or local excursions of the ribbon flux up to a scale size of $n = 360°/6° = 10$ can be clearly identified. Hence, the prior distribution for the ribbon flux $F_R(\theta, \phi)$ is controlled by parameters I, α, ω, and u, with I and u being controlled by precision parameters λ_I and λ_u. Thus, the prior model for the ribbon flux is

$$p(F_R) = p(I|\lambda_I)p(\lambda_I) \times p(\alpha, \omega) \times p(u|\lambda_u)p(\lambda_u).$$

Because of the *IBEX* orbit, one portion of the sky has been mostly viewed through the terrestrial magnetosphere, which can affect the heliospheric ENA flux and represents an additional, non-heliospheric source of ENA emission observable by *IBEX*. Because the ENA sky maps in this viewing region contain additional, non-heliospheric flux, this region of magnetospheric

obstruction is removed from the flux model by applying a flux mask $F_M(\theta, \phi)$ in this region as the second flux model component. Thus, the measured ENA flux in this region has no influence on the results of the statistical analysis, which interpolates the ENA flux within the magnetospheric obstruction based on the variation of the flux in pixels in the immediate vicinity outside the magnetospheric obstruction. Within this mask, the pixel values are allowed to vary freely, a priori. Outside the mask, the pixel flux values are set to a constant flux value $F_M(\theta, \phi) = 0$. Hence, the prior for the mask is $p(F_M) \propto 1$, as long as the pixel flux values outside of the mask are 0. This term ensures that possibly aberrant measurements taken near Earth's magnetosphere do not affect the statistical analysis.

The third component of the flux model $F_{RES}(\theta, \phi)$ accounts for the residual ENA flux that is not part of the ribbon and primarily consists of the globally distributed flux (McComas et al. 2009b; Schwadron et al. 2011). This is modeled as an isotropic Gaussian Markov random field (Besag et al. 1995), which incorporates a single precision parameter that accounts for spatial dependence in this flux, allowing for nearest neighbor dependence within the flux map $F_{RES}(\theta, \phi)$. By definition, the residual flux model is $F_{RES}(\theta, \phi) = F_{IBEX}(\theta, \phi) - F_R(\theta, \phi) - F_M(\theta, \phi)$, where, as before, $F_{IBEX}(\theta, \phi)$ is an ENA flux map from Figure 2. This induces a likelihood for the *IBEX* flux map that is controlled by the precision parameter λ_e

$$L(F_{IBEX}|F_R, F_M, \lambda_{RES})$$
$$\propto \lambda_{RES}^{n/2} \exp\left\{-\frac{\lambda_{RES}}{2} \sum_{i \sim j} (F_{RES,i} - F_{RES,j})^2\right\},$$

where $n = 60 \times 30$ is the number of pixels and the sum $\{i \sim j\}$ is over pairs of adjacent pixels in both azimuth and polar directions.

In regions of small ribbon flux (i.e., where $F_R(\theta, \phi) \approx 0$) outside of the magnetospheric obstruction mask (where, by definition, $F_M(\theta, \phi) = 0$), we have, by definition, $F_{RES}(\theta, \phi) = F_{IBEX}(\theta, \phi)$. The value of $L(F_{IBEX}|F_R, F_M, \lambda_{RES})$ in these particular regions is critical for estimating the spatial dependence of the non-ribbon flux via λ_{RES} in order to derive $F_{RES}(\theta, \phi)$ in regions of significant ribbon flux and within the magnetospheric obstruction mask.

The measured flux map F_{IBEX} at one energy passband and its associated flux model ($F_R + F_M + F_{RES}$) are coupled using a Bayesian framework, producing a multivariate posterior density describing uncertainty of the unknown flux model parameters. F_{IBEX} is a key, explicit component of the statistical framework,

whose posterior is given by

$$\pi(I, \lambda_I, \alpha, \omega, u, \lambda_u, \lambda_{RES}|F_{MAP}) \propto L(F_{MAP}|F_R, F_M, \lambda_{RES})$$
$$\times p(I|\lambda_I)p(\lambda_I) \times p(\alpha, \omega) \times p(u|\lambda_u)p(\lambda_u).$$

Samples from this highly multivariate posterior distribution are generated using Markov chain Monte Carlo (Robert & Casella 2004). The Markov chain was run for 30,000 iterations, saving every tenth realization. From these realizations, we derive posterior mean values and produce uncertainty intervals for each $6°$ azimuthal sector, in particular the polar angle $\bar{\phi}_{MAX}(\theta)$ of maximum ribbon flux around the ribbon of Figure 5 and the intensity function $I(\theta)$ of Figure 6. For the same realizations, the mean asymmetry parameter $\bar{\gamma}_l$ of the ribbon flux is likewise retained (Figure 7).

REFERENCES

Armstrong, J. W., Rickett, B. J., & Spangler, S. R. 1995, ApJ, 443, 209
Basu, M. 2002, ITSMC Part C, 32, 252
Besag, J., Green, P., Higdon, D., & Mengersen, K. 1995, StaSc, 10, 3
Burlaga, L. F., Ness, N. F., & Stone, E. C. 2013, Sci, 341, 147
Bzowski, M., Kubiak, M. A., Möbius, E., et al. 2012, ApJS, 198, 12
Canny, J. 1986, ITPAM, 8, 679
Casella, G., & Berger, R. 2002, Statistical Inference (2nd ed.; Belmont, CA: Duxbury)
Chalov, S. V., Alexashov, D. B., McComas, D., et al. 2010, ApJL, 716, L99
Dayeh, M. A., McComas, D. J., Livadiotis, G., et al. 2011, ApJ, 734, 29
Frisch, P. C., Andersson, B.-G., Berdyugin, A., et al. 2012, ApJ, 760, 2
Frisch, P. C., Redfield, S., & Slavin, J. D. 2011, ARA&A, 49, 237
Funsten, H. O., Allegrini, F., Crew, G. B., et al. 2009a, Sci, 326, 964
Funsten, H. O., Guthrie, A. A., Harper, R. W., et al. 2009b, SSRv, 146, 75
Fuselier, S. A., Allegrini, F., Funsten, H. O., et al. 2009, Sci, 326, 962
Grzedzielski, S., Bzowski, M., Czechowski, A., et al. 2010, ApJL, 715, L84
Hastie, T., Tibshirani, R., & Friedman, J. 2009, The Elements of Statistical Learning (New York: Springer)
Hebrard, G., Mallouris, C., Ferlet, R., et al. 1999, A&A, 350, 643
Heerikhuisen, J., & Pogorelov, N. V. 2011, ApJ, 738, 29
Heerikhuisen, J., Pogorelov, N. V., Zank, G. P., et al. 2010, ApJL, 708, L126
Heerikhuisen, J., Zirnstein, E. J., & Funsten, H. O. 2013, ApJ, submitted
Livadiotis, G., McComas, D. J., Randol, B. M., et al. 2012, ApJ, 751, 64
McComas, D. J., Alexashov, D., Bzowski, M., et al. 2012a, Sci, 336, 1291
McComas, D. J., Allegrini, F., Bochsler, P., et al. 2009a, SSRv, 146, 11
McComas, D. J., Allegrini, F., Bochsler, P., et al. 2009b, Sci, 326, 959
McComas, D. J., Barraclough, B. L., Funsten, H. O., et al. 2000, JGR, 105, 10419
McComas, D. J., Buzulukova, N., Connors, M.G., et al. 2012b, JGRA, 117, A03225
McComas, D. J., Dayeh, M. A., Allegrini, F., et al. 2012c, ApJS, 203, 1
McComas, D. J., Dayeh, M. A., Funsten, H.O., et al. 2013, ApJ, 771, 77
McComas, D. J., Funsten, H. O., Fuselier, S. A., et al. 2011, GeoRL, 38, L18101
Möbius, E., Bochsler, P., Bzowski, M., et al. 2012, ApJS, 198, 11
Möbius, E., Liu, K., Funsten, H., Gary, S. P., & Winske, D. 2013, ApJ, 766, 129
Pogorelov, N. V., Heerikhuisen, J., Zank, G. P., et al. 2011, ApJ, 724, 104
Ratkiewicz, R., & Grygorczuk, J. 2008, GeoRL, 35, L23105
Robert, C. P., & Casella, G. 2004, Monte Carlo Statistical Methods (2nd ed.; New York: Springer-Verlag)
Schwadron, N. A., Allegrini, F., Bzowski, M., et al. 2011, ApJ, 731, 56
Schwadron, N. A., Bzowski, M., Crew, G. B., et al. 2009, Sci, 326, 966
Schwadron, N. A., & McComas, D. J. 2013, ApJ, 764, 92
Slavin, J. D., & Frisch, P. C. 2008, A&A, 491, 53
Spangler, S. R., Savage, A. H., & Redfield, S. 2011, ApJ, 742, 30
Winkler, G. 2003, Image Analysis, Random Fields and Markov Chain Monte Carlo Methods: A Mathematical Introduction: Applications of Mathematics, Stochastic Modelling and Applied Probability, Vol. 27 (2nd ed.; Berlin: Springer-Verlag)
Zank, G. P., Heerikhuisen, J., Wood, B. E., et al. 2013, ApJ, 763, 20